CHEMISTRY OF MATERIALS

pubs.acs.org/cm

Article

High Selectivity toward Photoreduction of Carbon Dioxide to Methane over Copper-Doped Titania: Investigations Using Operando Techniques

Published as part of Chemistry of Materials special issue "C. N. R. Rao at 90".

Kaustava Bhattacharyya,* Chandrani Nayak, Dibyendyu Bhattacharyya, Ahin Roy, and Avesh K. Tyagi*

Cite This: *Chem. Mater.* 2025, 37, 3927−3949

Read Online

ACCESS | Metrics & More | Article Recommendations | Supporting Information

ABSTRACT: The photocatalytic reduction of CO_2 to CH_4 is a highly beneficial option from the perspective of both energy and the environment. Several promising photocatalysts that selectively produce CH_4 (C1) mainly comprise Cu in different oxidation states. Since the CO_2 reduction to CH_4 is an 8 electron reaction, the formation of the different intermediates upon adsorption and photocatalytic reaction had to be discerned individually. Earlier, it has been demonstrated by our group that the Cu-doped TiO_2 photocatalyst is able to selectively reduce CO_2 to CH_4 with very good yield. The present article reports detailed in situ FT-IR studies to delineate the different intermediates formed by exposure to CO_2 and moisture over the Cu-doped TiO_2 catalysts like bidentate carbonates, monodentate carbonates, bicarbonates, and carboxylates identified over different Cu-doped TiO_2 surfaces. These intermediates were correlated with the differential electron densities over Cu, Ti, and O vacancies ascertained from XANES/EXAFS (XAS) studies. These catalysts were then selectively reduced within the in situ FT-IR chamber to further ascertain the role of the Cu^{1+}, Ti^{3+}, and O vacancies to rationalize the effect of different Lewis base sites in the photocatalysts. In situ XAS studies in correlation with the in situ FT-IR studies lead to a generic understanding of different adsorbate species formed over the Cu surfaces at the molecular level. The time-dependent XAS studies used for the photoreduction of CO_2 over the Cu-doped photocatalysts were undertaken to establish the precise role of Cu and to delineate the alteration in the bond distances on the photocatalytic reduction of CO_2. This study principally delineates the effect of Cu sites for the photocatalytic CO_2 reduction process in the presence of moisture as compared to the other probable active sites present in the photocatalyst. The effect of oxidation states and the formation of different intermediates for reactive adsorption and, in turn, their effect on photocatalysis will pave the way to formulate further better photocatalysts for the photoreduction of CO_2.

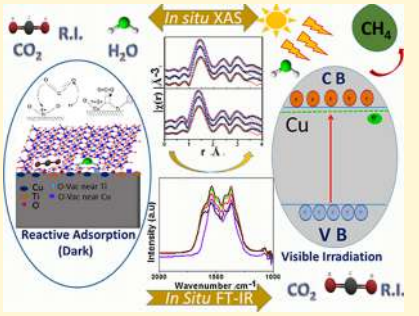

1. INTRODUCTION

In the present world, where the depletion of fossil fuels has become a major concern, the search for alternative methods to produce fuels has attracted considerable attention. Photocatalytic reduction of CO_2 has emerged as an important technique in this regard as it produces renewable and sustainable fuel from greenhouse gases like CO_2. The consumption of fossil fuels leads to the emission of CO_2, which, with a water- and sunlight-driven photocatalyst, can again be converted to fuel. This, therefore, ensures not only the production of fuel but also effective utilization of CO_2, which is responsible for global warming. In the process of semiconductor-mediated photocatalysis, the formation of holes (h^+) and electrons (e^-) is the fastest (femto-second regime) step, and comparably, the transfer kinetics along with the quenching dynamics of (h^+/e^-) by surface/bulk states are quite slow (nanosecond regime). Nevertheless, for mechanistic understanding apart from time domain kinetics, the (h^+/e^-) pathway mediated by structural properties along with knowledge of stable intermediates for photocatalysts is equally important.

Recently, considerable studies have been reported on the photocatalytic reduction of CO_2,[1−3] where several materials have been utilized, which comprise metal oxides, like titania (TiO_2),[4−6] zinc oxide (ZnO),[5] copper oxide (Cu_2O),[7] bismuth-based catalysts ($BiVO_4$),[8] chalcogenides cadmium sulfide (CdS),[9] layered materials like graphitic carbon nitride ($g\text{-}C_3N_4$),[10] multiwalled nanotubes,[11] and double-layered hydroxides.[12] The redox potential for a single electron transfer to CO_2 is −1.85 eV (vs NHE at pH = 7). This high value stems from the fact that bending a linear CO_2 molecule and injecting an electron

Received: March 14, 2024
Revised: February 6, 2025
Accepted: February 7, 2025
Published: February 21, 2025

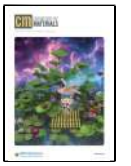

Table 1. Comparison of Different Photocatalysts Used for CO_2 Reduction with the Product of CH_4[a]

photocatalyst	reactants	light source	major product	formation rate of CH_4 (μL/h/g)	ref
CuO−TiO_2 (hollow microspheres)	CO_2 and H_2O	Hg lamp, 40 W, 254 nm	CO and CH_4	46.36	29
Pd/TiO_2	CO_2 and H_2O	500 W Hg lamp	CH_4 and CO	25.648	30
CdS/TiO_2 film	CO_2 and H_2O	350 W Xe lamp	CH_4	266.7	31
MoS_2/TiO_2 fibers	CO_2 and H_2O	350 W Xe lamp	CH_4	515.2	32
$ZnIn_2S_4$/TiO_2 nanobelts	CO_2 and H_2O	350 W Xe lamp	CH_4	25.4	33
mesoporous (p−n)-type Cu_xO−TiO_2 (x = 1, 2)	CO_2 in He bubbled through H_2O	100 W xenon solar simulator	CH_4	221.63	21
Cu-doped TiO_2 (present work)	CO_2 and H_2O	(350−700) nm WLS ∼ 234 mW/cm^2	CH_4	1081	22
Pt_2/3-DOM-$SrTiO_3$	CO_2 and H_2O		CH_4	26.7	34

[a]3-DOM = three-dimensional ordered mesoporous materials; (p−n)-type = (p−n)-type heterojunction material; WLS = white light source with a range of 350−700 nm, a peak at ∼430 nm, and a flux of ∼234 mW/cm^2.

into its antibonding orbitals is unfavorable.[3] The multielectron step becomes a bottleneck for the production of CH_4 and higher C_2 products.

In both photocatalytic and electrophotocatalytic CO_2 reductions, Cu- and Cu-doped systems play a strong part.[13] However, the exact role of Cu in the photocatalytic reaction is still not understood clearly. The role of the Cu is still quite debatable in the scientific community, and there are still differences over the exact role of Cu^{1+}, Cu^{2+}, and Cu^0 species for the effective CO_2 reduction. A few reports point toward Cu^{2+} and Cu^0 species as active sites,[14] while others reported Cu^{1+} as the most active site[15,16] for CO_2 photoreduction. The Cu species (Cu^0 and Cu^{2+}) were successfully incorporated on TiO_2 supports and then evaluated for their potential to hydrogenate CO_2 by Chen et al. A Cu-loaded TiO_2 enhances the amount of Ti^{3+} relative to Ti^{4+} in the photocatalyst, which promotes the photohydrogenation of CO_2.[17] The coexistence of Cu/Cu^{1+} species during the photoreaction enhances photocatalytic efficiency by increasing the lifetime of electrons, leading to the enhancement of CO_2 hydrogenation.[18] Tashibi et al. have shown that Cu-doped TiO_2 reduces CO_2 photocatalytically to CH_4, H_2, and CO. In this study, the photocatalytic reduction of CO_2 decreased in the presence of Cu/TiO_2 in comparison to pure TiO_2.[19] The authors associated this with the formation of the CuO phase acting as a recombination center by this group. Maximum CH_4 was obtained by the TiO_2 photocatalyst (9.3 μL/g/h). Wu et al. synthesized Cu-doped TiO_2 and showed that a lower concentration of Cu-doping was better; however, the yield for the product of CH_4 was quite low (∼0.6 μL/g/h).[20] Park et al. showed a mesoporous (p−n)-type heterojunction material, Cu_xO−TiO_2 (x = 1, 2), synthesized via heating of Cu/Cu_2O nanocomposites mixed with a TiO_2 precursor. These materials showed rapid charge separation because of the intrinsic p−n heterojunction nature of the material for the CO_2 reduction with a remarkable methane yield of 44.8 μL/g/h. No metal cocatalysts are utilized in the above set of CO_2 reduction reactions.[21]

In the recent past, our group has shown that the oxidation state of Cu (Cu^{1+}) and the O vacancies created by doping Cu in the anatase TiO_2 system play the most important role in the selective photocatalytic reduction of CO_2 to CH_4.[22] These Cu-doped TiO_2 photocatalysts [Cu-(1 to 10) atom %] synthesized by the sol−gel converted the reactant mixture of CO_2 and moisture selectively into methane and oxygen under visible irradiation without the use of any sacrificial agent or any cocatalyst, where the lowest doping (Cu-1%) concentration in the TiO_2 lattice shows the maximum production of CH_4 (1081 μL/h/g), whereas the highest doping (Cu-10%) shows the least activity (200 μL/h/g).[23] There are two distinct types of Cu^{2+} species in the doped system, and clustering of the Cu^{2+} states at higher doping concentrations may be detrimental for the photoactivity. The electronegative surface Cu^{1+} species along with the O vacancies seem to play the most important role in the photocatalytic reduction of CO_2 to CH_4. Since the formation of CH_4 is an 8 e^- reaction, it is inherently complicated to understand the adsorption mechanism and the photocatalytic mechanism together. The present article delineates the different intermediates formed by the adsorption of CO_2 and moisture over the different Cu-doped photocatalysts and later tries to identify the role of Cu in the photocatalytic mechanism of the CO_2 reduction to CH_4 using an operando EXAFS technique in conjunction with an in situ FT-IR technique. It has been unequivocally shown that Cu plays a very strong role in the reaction of CO_2 to CH_4 for the Cu-doped TiO_2 systems.

Currently, there has been a good endeavor to detect the different intermediates formed over the catalyst's surface using FT-IR. Tagwa et al. showed formate intermediates over CO_2 reduction by H_2 over Cu/TiO_2 catalysts.[23] Wu et al. on photocatalytic reduction of CO_2 on TiO_2 and Cu/TiO_2 photocatalysts showed carbonate and bicarbonate on adsorption and formic acid, dioxymethylene, formaldehyde, and methoxy species upon reaction.[24] Ferrari et al. showed the formation of carbonates on CO and CO_2 adsorption on the anatase TiO_2 samples, and different intermediates were correlated with density functional theory (DFT) calculation, showing surface energy effects for the formation of surface carbonates over the TiO_2 anatase (0 0 1) plane.[25] Bhattacharyya et al. showed reactive adsorption of CO_2 on oxidized, reduced, and platinized TiO_2 nanotubes (Ti-NTs) and Pt-TiNTs.[26] These intermediates formed over the catalytic surface were studied and correlated with X-ray photoelectron spectroscopy (XPS) data to assign them for acid−base reactions by the surface Lewis basic sites with the different intermediate acidic states.[26] Illumination on the activation and dissociation of CO_2 was investigated at 190 and 300 K on titania-supported noble metals, which showed photoinduced dissociation of CO_2 (through the formation of CO_2^-) resulting in CO formation on Pt/TiO_2, Rh/TiO_2, and Ir/TiO_2; however, no CO was observed on Pd/TiO_2 and Ru/TiO_2.[27] CO_2 adsorption on $Ti_3O_6^-$, which serves as a model for an oxygen vacancy on a titania surface, was studied using infrared photodissociation (IRPD) spectroscopy in combination with density functional theory (DFT) and coupled cluster computations, showing the formation of certain types of carbonate anions.[28]

https://doi.org/10.1021/acs.chemmater.4c00748
Chem. Mater. 2025, 37, 3927−3949

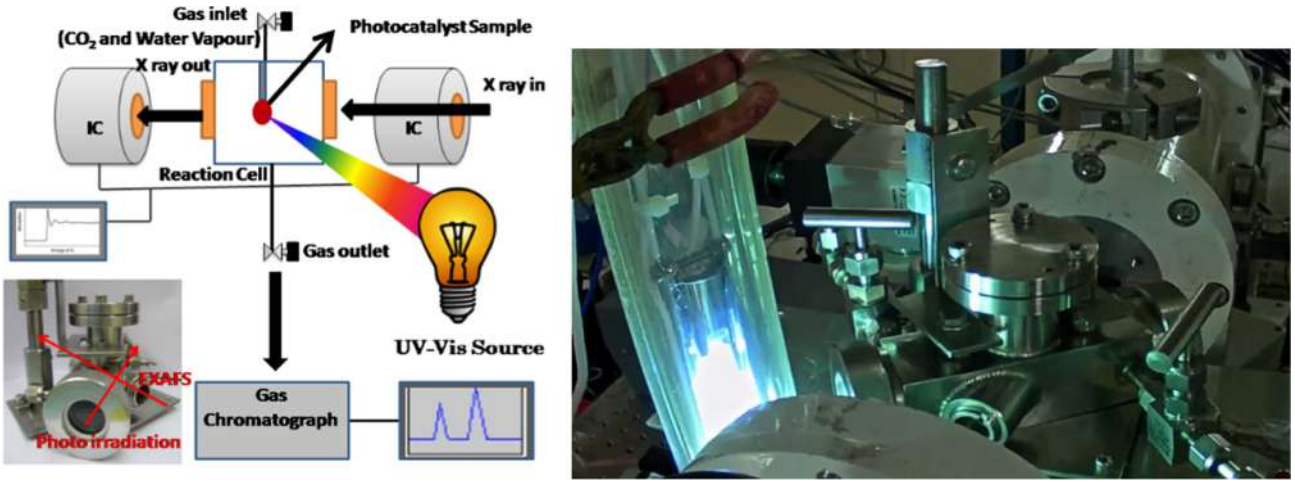

Figure 1. Schematic diagram of the experimental setup for in situ XAS measurement during photocatalytic reactions along with the photograph of the reaction cell and actual photograph of the experimental setup for in situ XAS measurement during photocatalytic reactions.

Though there are few studies on the adsorption of CO_2 over a catalytic surface, CO_2 reduction, however, not only involves CO_2 adsorption over the catalytic surface but also involves the adsorption of moisture over the surface, leading to different intermediates. To the best of our knowledge, this is the first time the effect of adsorption and reaction of CO_2 and moisture has been investigated in totality. The present work highlights direct evidence of electrons being transferred through Cu^{1+} during the process of photocatalysis and how effective formation of carboxylates during adsorption of CO_2 and H_2O helps in CO_2 reduction. This study not only shows the different intermediates formed over Cu-doped TiO_2 but also establishes the effect of moisture adsorption on these catalysts and deciphers the different intermediates formed over the reduced surface having Cu^{1+} or O vacancies.

The above table (Table 1) showcases our photocatalyst to be one of the best photocatalysts, highly selective in nature, and in turn, it is important to establish the detailed mechanism of CO_2 reduction in Cu-doped TiO_2

2. EXPERIMENTAL DETAILS

2.1. Synthesis of Cu-Doped TiO_2 Photocatalysts. Various Cu-doped TiO_2 catalysts were synthesized by a modified sol−gel process in which the required stoichiometric amount of Cu $(NO_3)_2{\cdot}3H_2O$ (Aldrich, 97%) was initially dissolved in nanopure water at room temperature and neutral pH. The copper nitrate solution was maintained at 0 °C by external application of an ice−salt mixture. Ti(IV) iso-propoxide solution in iso-propanol (IPA) was added to the copper nitrate solution, dropwise in a controlled manner over a period of 1 h, with vigorous stirring until the formation of a uniform gel. This gel was stirred further for 1 h to ensure the incorporation of a copper precursor in the titanium gel phase. The gel was kept for nucleation for 12 h in the dark, and then IPA was removed by keeping the gel in a Petri dish for 12 h. The mass was then dried in an oven at 100 °C for 4 h. The resulting solid mass was crushed and calcined at 500 °C for 3 h. The required amount of Cu (5 and 10 atom %) doping was achieved by adding a stoichiometric amount of copper nitrate solution and Ti(IV) iso-propoxide. Subsequently, in this article, the 1%, 5%, and 10% Cu-doped TiO_2 samples would be referred to as Cu-1, Cu-5, and Cu-10, respectively. The amount of Cu doped in the samples, both bulk and surface, is reported in Table S3. The virgin nano TiO_2 (anatase) was synthesized in a similar fashion and is denoted as nano-TiO_2.

2.2. Photocatalytic Reduction of CO_2. For the photocatalytic reduction of CO_2, the Cu-doped TiO_2 sample was loaded into the photocatalytic reaction cell, which has been discussed later. 300 mL of CO_2 and 16 mL of water vapor were inserted into the cell. The catalyst sample was illuminated with visible radiation, and the photocatalysis reaction was monitored for 8−12 h by in situ XAS measurements at both Ti and Cu K-edges. The white light source simulating the visible spectrum emits in the 350−700 nm range with a peak around 430 nm and a flux of ∼234 mW/cm^2. The photon flux as measured by the uranyl oxalate actinometer was found to be $\sim 6.5 \times 10^{14}$ photons/cm^2/s. The product gases were monitored every hour during the reaction using the gas chromatograph.

2.3. In Situ FT-IR Reaction Experiments. The in situ FT-IR experiments were conducted over Bruker Vertex 70 V with an external unit (model name: XAS) for conducting in situ FT-IR experiments in transmission mode in the 4000−1000 cm^{-1} range with a mercury−cadmium−telluride (MCT) detector, medium band, LN_2-cooled with a spectral range of 12,000−600 cm^{-1} having detectivity $D^* \sim 2 \times 10^{10}$ or better and a hold time of 12 h. An external unit with a SPECAC cell was used as the in situ FT-IR cell attached on the right side of the main unit and had a typical dimension of around [25 (W) × 27 (D) × 17 (H)] cm^3. The high-vacuum facility was attached with a turbomolecular pump (air-cooled) coupled to a dry roughing pump and equipped with appropriate digital pressure sensors. The typically achieved vacuum level was 10^{-6} mbar or lower, programmable controlled temperature up to 800 °C, and pressure range from ∼10^{-6} mbar to ∼50 bar along with required safety features. An in situ cell in transmission, specular, reflectance, and decomposition mode with chemically resistant stainless steel fitted with suitable windows and with the provision of at least three inlet and outlet ports for the evacuation and introduction of gases was used. A suitable cooling facility for the reaction cell was present. The window assembly of ZnSe and KBr and the transmission/decomposition holder were employed. A suitable temperature programmer/controller for sample heating up to 800 °C with a temperature accuracy of ±1 °C was provided.

Initially, the catalysts were ground in a mechanical grinder and then pelletized to form a self-supported pellet without the use of any binder. The pellet was placed in the transmittance in situ cell in the required groove and was then subjected to 10^{-4} mbar pressure and ∼100−350 °C as a function of temperature (with an increment of 50 °C) for around 3−6 h in order to clean the surface of the pellet. A pellet spectrum was recorded at 50 °C to understand the temperature effect over the pellet. The pellet was then exposed to 5−10 cc of 99% pure CO_2, which was placed in the in situ cell through the injection syringe from the septum, thus breaking the vacuum. The spectra of adsorbed CO_2 were recorded as a function of time. Similarly, for the moisture and CO_2 experiment, the pellet was cooled to room temperature, and high vacuum was initially exposed to the 5−15 cc vapor taken in a syringe when the water was boiled in a closed container and subsequently exposed to different volumes of CO_2. After the reactive adsorption of the CO_2 and moisture, the cell was evacuated using the turbo molecular

https://doi.org/10.1021/acs.chemmater.4c00748
Chem. Mater. 2025, 37, 3927−3949

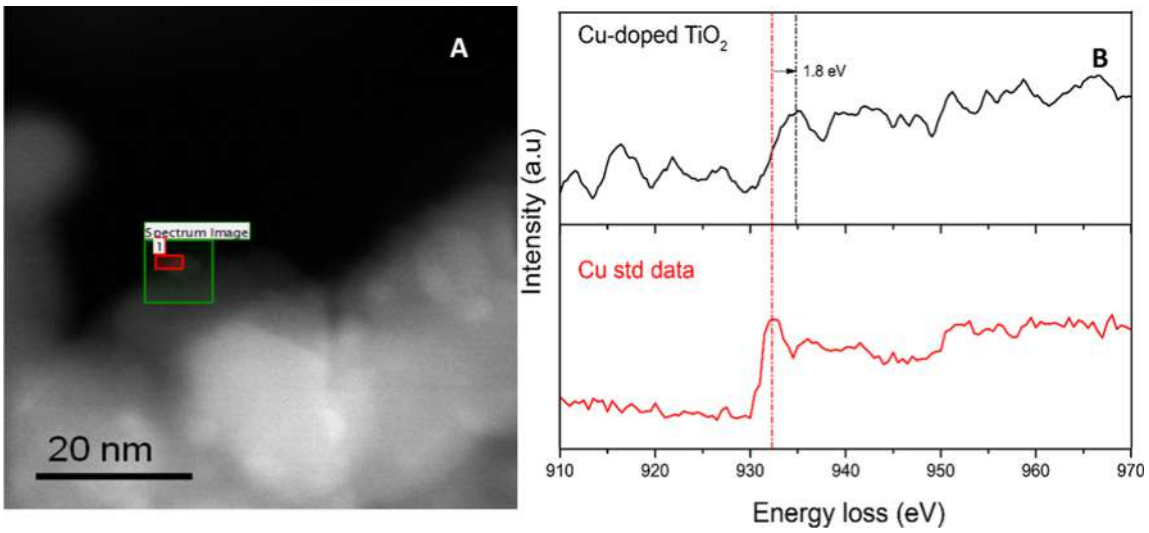

Figure 2. (A) Image for EELS mapping Cu K-edge of Cu-doped TiO_2; (B) comparative EELS edge plot for Cu standard data and the Cu EELS data in Cu-doped TiO_2.

pump (TMP) to attain a vacuum of around $\sim 10^{-3}$ mbar to understand the strength of the intermediates formed (labile or strongly adsorbed on the catalytic surface). Subsequently, these catalysts were reduced in situ in order to increase the Cu^{1+} state in the catalyst with the reduction mixture of Ar and H_2 (50 cc) at a temperature of ~150−175 °C. After reduction with the reduction mixture, these catalysts were exposed to CO_2 and moisture to understand the reactive adsorption of them on the reduced catalyst.

2.4. In Situ X-ray Absorption Spectroscopy Setup for Photocatalytic Reactions. The experimental setup for in situ XAS measurements during photocatalytic reactions consists of a specially designed reaction-cum-measurement cell which comprises quartz and glass windows for shining UV and visible radiation on the sample in addition to the Kapton windows for X-ray transmission. Two valves are provided at the inlet and outlet of the chamber so that it can be converted to a closed reactor for studying the photocatalytic reactions discussed in this study. Measured proportions of CO_2 and water vapor were taken in syringes and inserted in the chamber through an inlet port blanked with a septum, while the measured amount of the product gases was periodically collected in a syringe from the chamber through an outlet port blanked with a septum and was fed to a computer-controlled gas chromatograph (Netel, India make). The product gases (CO_2 and CH_4) were detected using a Porapak N column and using He as a carrier gas for gas chromatography (GC). For the photocatalytic reaction, a 250 W white light lamp with a wavelength range of 350−700 nm and a luminous flux of 35,000 Lm was used to shine light on the catalyst sample placed inside the chamber through a quartz window. The schematic of the experimental setup along with the photograph of the reaction cell and experimental setup is shown in Figure 1. This setup was used to study photocatalytic reduction of CO_2 using 5% and 10% Cu-doped TiO_2 as a catalyst.

Time-resolved X-ray absorption spectroscopy measurements of the catalyst samples at Cu and Ti K-edge were carried out in transmission mode at the Scanning EXAFS Beamline (BL-9) at the Indus-2 Synchrotron Source (2.5 GeV, 100 mA) at the Raja Ramanna Centre for Advanced Technology (RRCAT), Indore, India.[8,9,35,36] The beamline uses a double crystal monochromator (DCM), which works in the photon energy range of 4−25 keV with a resolution of 10^4 at 10 keV. A 1.5 m horizontal premirror with meridional cylindrical curvature was used prior to the DCM for collimation of the beam and higher harmonic rejection. The second crystal of the DCM is a sagittal cylinder with a radius of curvature in the range of 1.28−12.91 m, which provides horizontal focusing to the beam. Generally, by using the step-by-step scanning of the DCM, a typical XAS data in this beamline takes 30 min in case of transmission mode measurement and 1 h for fluorescence mode measurement. However, continuous scan XAS measurements were undertaken by which the data acquisition time could be reduced substantially, retaining the advantage of high resolution offered by the step-by-step scan of a double crystal monochromator, and therefore, it can now be used for in situ studies. In this mode, a full EXAFS scan was taken in 5 min, while XANES data can be acquired in less than 1 min. For the in situ XAS measurements in transmission mode, the reaction chamber with the sample was placed between two ionization chamber detectors. For Cu K-edge measurements, 50 mg of the catalyst samples was pelletized, and for Ti K-edge measurements, 20 mg of the samples was uniformly spread over a Kapton tape. The first ionization chamber measures the incident flux (I_0), and the second ionization chamber measures the transmitted intensity (I_t), and the absorbance of the sample is obtained as $\left(\mu = \exp\left(-\frac{I_t}{I_0}\right)\right)$.

2.5. Characterization. The powder sample was dispersed in isopropyl alcohol (IPA) and was drop-casted on holey-carbon-coated 400-mesh Ni grids, followed by drying by the evaporation of the IPA. The STEM imaging was carried out in a JEOL Grand ARM machine, operated at 300 keV and fitted with an image and probe corrector, a single-window JEOL EDS detector, and a postcolumn Gatan EELS spectrometer. The convergence angle of the corrected probe for the STEM-HAADF imaging was 25 mrad, and the collection angle of the EELS spectrometer was 26 mrad. The dual time of the beam for EELS spectrum imaging was 16 ms px^{-1}. To elucidate the electronic states of the photocatalysts, X-ray photoelectron spectroscopy (XPS) and X-ray Auger electron spectroscopy (XAES) studies were performed in the SPECS instrument with a PHOBIOS 150 delay line detector (DLD) employing an Al Kα (1486.6 eV) dual anode as an X-ray source (power: 385 W, voltage: 13.85 kV, sample current: 175.6 nA) at a pass energy of 50 eV. The EPR spectra were recorded in a Bruker EMX series spectrometer operating at the X band with a 100 kHz modulation frequency. DPPH (g = 2.0036) was used as a standard for the g-value. The sample amount was limited to 20 mg so as to have a minimum temperature variation over the length of the sample for low-temperature EPR. Typical experimental parameters were as follows: modulation amplitude: 1 G, microwave power: 7 mW, time constant: 40.96 ms, and conversion time: 40 ms. Laser Raman spectra were recorded on a LABRAM-1 spectrometer (ISA) in the backscattering geometry and at a spectral resolution of 2 cm^{-1}. An Ar^+ ion laser (488 nm) was used as an excitation source.

3. RESULTS AND DISCUSSION

3.1. X-ray Diffraction Studies. Figure S1 shows XRD data for the above-synthesized materials, which initially shows that all of the above-synthesized photocatalysts are single phasic and

https://doi.org/10.1021/acs.chemmater.4c00748
Chem. Mater. 2025, 37, 3927−3949

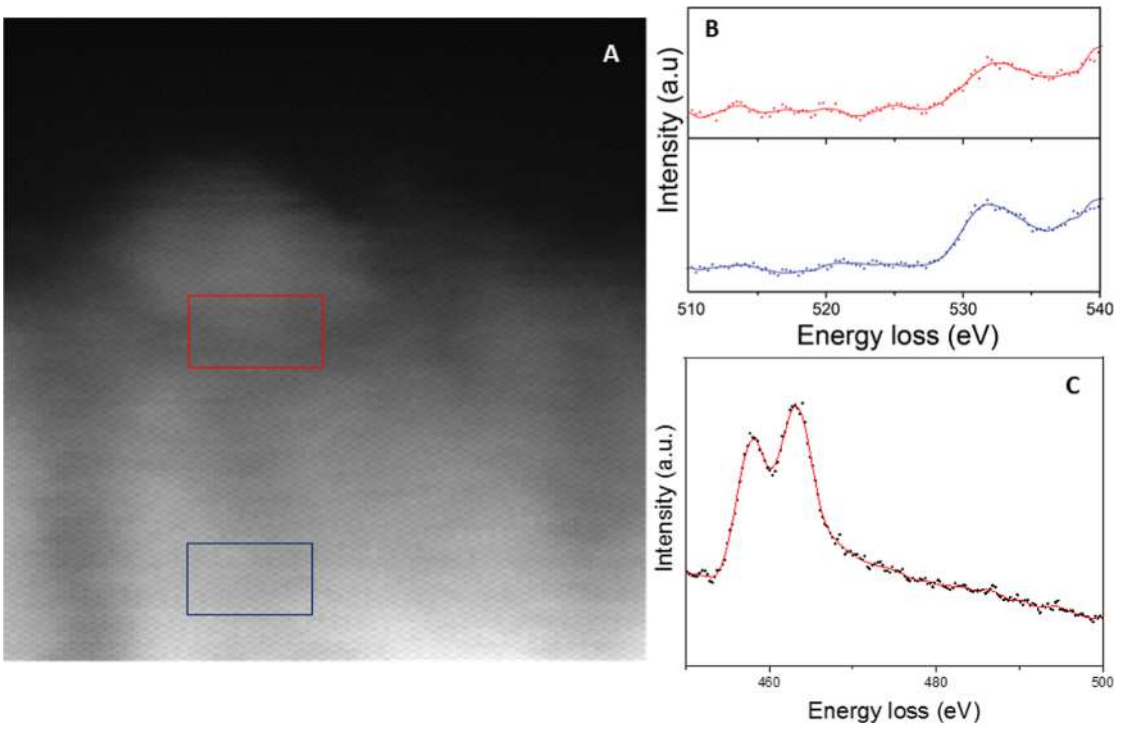

Figure 3. (A) EELS mapping with the O K-edge for the Cu-rich area and Ti-rich area; (B) O K-edge peaks in Cu-rich and Ti-rich areas. (a) Red color is the Cu-rich area; (b) blue color is the Ti-rich area; (C) EELS data of Ti from the Cu-rich Ti region (red area).

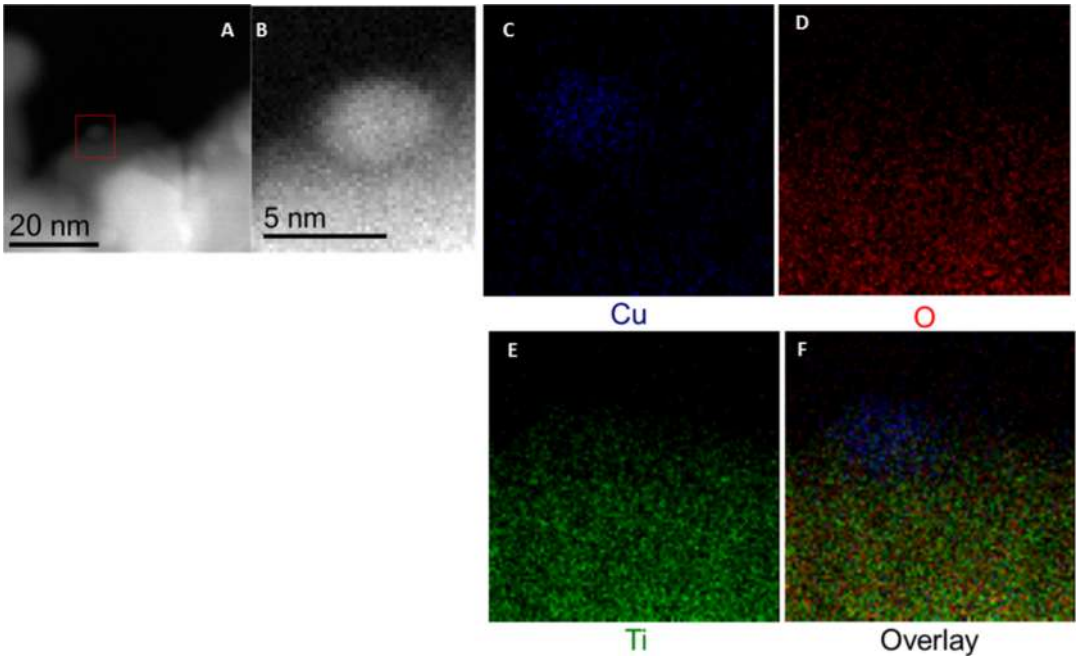

Figure 4. Elemental mapping from the EDS spectra of the STEM picture. (A) Low-magnification image of the same area from which EDS is carried out. (B) EDS is carried out on the area. Elemental mapping for (C) Cu; (D) O; and (E) Ti. (F) Overlay of the elemental mapping.

that all of them possess the anatase TiO_2 structure. The XRD pattern corresponding to nanotitania is found to match with that of the bulk, tetragonal anatase phase (JCPDS 21-1272). It can be inferred that the synthesized product is TiO_2 in the tetragonal anatase phase. The effect of substitutional doping of Cu^{2+} in the TiO_2 anatase lattice shows certain distinctive features. The XRD patterns of the [Cu-1, Cu-5, and Cu-10]-doped samples do not show any characteristic signature of the CuO, Cu_2O, or Cu phase. This indicates that all the samples possess a phase-pure anatase structure. Though all the XRD patterns (for the Cu-doped samples) show a single-phase character, the XRD lines of the nanotitania and Cu-doped titania samples exhibit significant broadening as compared to the parent anatase TiO_2. The coherently diffracting domain sizes calculated using the Scherrer equation from the broadening of the fwhm of the (101) peak are shown in Table S1. The crystallite size of nano (Cu-0 and Cu-100) is about 20 nm. The average crystallite size of the Cu-

https://doi.org/10.1021/acs.chemmater.4c00748
Chem. Mater. 2025, 37, 3927−3949

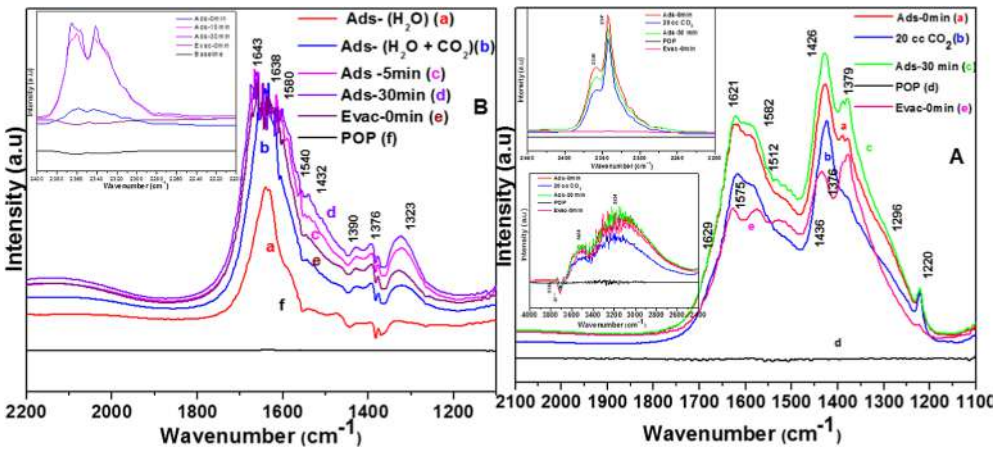

Figure 5. (A) Adsorption of CO_2 over the nano-TiO_2 surface shows vibrational data from 2000 to 1100 cm^{-1}, and the inset shows vibration bends in the range of 4000−2400 cm^{-1} as well as in the range of 2400−2200 cm^{-1}; the designated bend for CO_2 for the samples is as follows: (a) adsorption: 0 min; (b) 20 cm^3 CO_2 adsorption; (c) adsorption: 30 min; (d) pellet on pellet (POP); and (e) Evac: 0 min. (B) Adsorption of CO_2 and H_2O over the nano-TiO_2 surface vibrational bending (2000−1100 cm^{-1}), and the inset shows bands in the range of 2400−2200 cm^{-1}; the designated bend for CO_2 is as follows: (a) adsorption of H_2O; (b) adsorption of H_2O and CO_2; (d) adsorption after 5 min; (e) adsorption after 30 min; (d) evacuation after 0 min; and (f) pellet on pellet.

doped TiO_2 [Cu-1 to Cu-10] materials is ∼18.2 nm. Details of XRD studies have been reported in our earlier paper.[22]

3.2. STEM and EELS Mapping. Figure 2A shows the mapping image for EELS with the Cu K-edge, and Figure 2B shows the EELS spectra of the Cu−K-edge for the general Cu-standard taken from the Gatan database and that of Cu as obtained from the Cu-doped TiO_2 sample (Cu-5). There is a clear shift of 1.8 eV of binding energy for the Cu-doped TiO_2 sample as compared to that of the Cu-standard sample, showing that the Cu cation is doped in conjunction with the XPS data set (FigureS 2), which shows the presence of Cu^{1+} and Cu^{2+}. In Cu-doped TiO_2, on moving to the Cu-rich compositions, the ratio of O prepeak to the K-edge of the O clearly increases. This indicates the introduction of O vacancies on doping Cu near the Cu centers. This data, coupled with the XPS data found in Figure S2C, clearly shows the presence of O vacancies in the Cu-doped TiO_2 lattice instead of a separate phase. This is clear proof of the formation of O vacancies along with that of XPS and indirectly by XRD results. The STEM-EELS mapping in Figure 3C shows clear Ti L-2,3 edges, which indicate the doping of Cu rather than separation. The elemental mapping from the STEM-EDS shown in Figure 4 clearly indicates the Cu doping in the TiO_2 system, evident from the Cu and Ti maps (Figure 4C,E) and the overlaid signals (Figure 4F).

3.3. In Situ FT-IR Studies for CO_2 Adsorption and CO_2 and H_2O Adsorption. *3.3.1. Nano-TiO_2.* The FT-IR spectrum of nano-TiO_2 upon exposure to CO_2 (Figure 5B) shows mainly the vibrational peaks in the bending region of 2000−1100 cm^{-1} where the peaks were obtained at 1621,1589, 1516, 1560, 1428, 1375, 1328, 1313, 1296, and 1220 cm^{-1}. The peaks present at 1589, 1516, and 1375 cm^{-1} show mainly the presence of bidentate carbonates (BDCs) as has been obtained for CO_2 adsorption over TiO_2 heated at 350 °C samples.[37−39] The vibrational bands corresponding to 1621, 1560, and 1428 cm^{-1} show the presence of bicarbonates (BCs), which are previously observed over CO_2 adsorption over TiO_2 and α- Cr_2O_3.[40,41]

A peak at 1220 cm^{-1} has also been previously observed on the γ-Al_2O_3 surface, which was assigned to bicarbonates by Mul et al.[42] The strong peak at 1296 cm^{-1} has been assigned to a bridging carbonate based on the observation of CO_2 absorptions on Ga_2O_3.[27] The vibrational bands in the region (4000−2400 cm^{-1}) (Figure 5B) mainly show peaks at 3517 and 3143 cm^{-1}, which represent the surface −OH groups that are liberated for the adsorption of CO_2 over the nano-TiO_2 surface, which has long been proved by our group in the recent past.[43] There are negative bands present at 3711 and 3735 cm^{-1}, which show usage of the surface −OH groups of TiO_2 for the adsorption of CO_2 to form reactive intermediates over its surface. Upon evacuation, the peaks are found at 1629, 1577, 1525, 1328, and 1313 cm^{-1} [Figure 5A(d)]. All these peaks correspond to the presence of the BDCs, which show that BDCs are very strongly bonded over the nano-TiO_2 surface. Also, the peaks for the bicarbonates are missing after evacuation, showing that these are mainly labile species formed over the nano-TiO_2 surface. Similarly, the intensity of bands at the stretching region lowers to 3508 and 3185 cm^{-1}, showing that different types of surface −OH were produced, among which some are labile and others are very strongly held on the nano-TiO_2 surface.

The adsorption of CO_2 over the H_2O-adsorbed surface of nano-TiO_2 is shown in Figure 5B. The exposure of CO_2 over the H_2O-adsorbed TiO_2 surface displays several additional intermediates. The major vibrational peaks obtained in the bending region are at 1643, 1638, 1580, 1540, 1432, 1390, 1370, and 1323 cm^{-1}, respectively. The band at 1638 cm^{-1} is formed just after the adsorption of H_2O (Figure 5B(a)), showing the presence of bending vibration of the surface −OH group over nano-TiO_2. An absorption at 1376 and 1390 cm^{-1} has been previously reported on both the Cr_2O_3 surface and the rutile TiO_2 surface, which are assigned for bidentate carbonates.[43] Strong absorptions are also observed at 1424 and 1553 cm^{-1}, which are assigned to bicarbonates.[40,44] The bands at 1580 and 1643 cm^{-1} are assigned for the bidentate carbonates.[40,43,45] In the stretch region (not shown here), there are a few additional bands that appear at 2871 cm^{-1}, which is a broad one along with the stretch bands obtained at 3528 and 3229 cm^{-1}, which show different types of surface-saturated −OH groups here also. The bicarbonate bands disappear upon evacuation, showing them to be labile species; on the other hand, the BDC bands are still present after the evacuation, showing them to be the strongly bound species. In order to understand the intermediates formed

https://doi.org/10.1021/acs.chemmater.4c00748
Chem. Mater. 2025, 37, 3927−3949

after reactive adsorption of CO_2 on the Cu-doped TiO_2 photocatalysts, the in situ FT-IR studies were conducted over Cu-1 catalysts.

3.3.2. TiO_2 (1% Cu). 3.3.2.1. Adsorption of CO_2 on 1% Cu-Doped TiO_2 (Cu-1). The reactive CO_2 adsorption on the Cu-1sample under ambient conditions (Figure 6) initially shows a

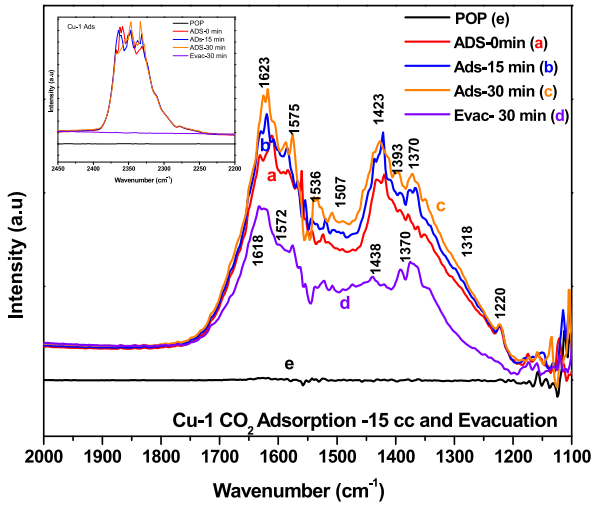

Figure 6. Adsorption of CO_2 over the Cu-1 surface; (a) adsorption after 0 min; (b) 15 min; (c) 30 min; and (d) evacuation: 30 min; (e) pellet over pellet inset shows the CO_2 peaks at the vibrational range of 2400−2200 cm^{-1}.

negative peak at 3718 cm^{-1}. The negative band primarily arises due to the usage of surface −OH groups by Cu-doped TiO_2 catalysts in order to attach to CO_2 over the catalytic surface as different carbonates, carboxylates, bicarbonates, etc. There are two very broad bands present at 3533 and 2989 cm^{-1} (not shown here),[46] indicating the adsorbed −OH and H_2O bands present in CO_2.

The CO_2 peaks were observed at 2345 and 2334 cm^{-1} along with increasing intensity as a function of the volume of CO_2 adsorbed on the surface. There are several other peaks at 1623, 1618, 1587, 1576, 1538, 1508, 1427, 1397, 1370, 1352, and 1223 cm^{-1} as presented in Figure 6. Here, the peaks at 1587 and 1576 cm^{-1} are representing bidentate carbonates (BDCs), as has been observed for CO_2 adsorption over the anatase TiO_2 sample.[40,43,46−49] The peaks originating at wavenumbers 1397, 1370, and 1352 cm^{-1} generally represent monodentate carbonates (MDCs),[39,41−43,45,50] and the peak at 1223 cm^{-1} is due to the surface bicarbonate.[41,47,51] The peaks belonging to 1623 cm^{-1} are mainly due to carboxylate[52] and 1618, 1538, and 1425 cm^{-1} due to bicarbonates. Apart from these peaks, the CO_2 peaks at 2345 and 2334 cm^{-1} are also present with an increase in intensity as a function of CO_2 concentration.

Upon evacuation, the FT-IR peaks were obtained at 1632, 1620, 1578, 1561, 1525, 1507, 1449, 1392, 1376, and 1345 cm^{-1} (Figure 6d). Initially, the −OH group bands are shifted to 3544 and 2929 cm^{-1}.[53] This is primarily due to the fact that the peaks earlier observed (Figure 6) correspond to labile −OH stretch frequencies along with −OH stretch frequencies for the strongly adsorbed −OH groups. This clearly indicates the presence of two types of surface −OH groups: physisorbed (labile ones) and those which are chemisorbed (strong ones). The nature of the surface −OH groups has a strong bearing on photocatalytic activity. The catalysts with higher chemisorbed −OH groups will have higher photocatalytic activity since these will bind with the reactive moieties to produce surface intermediate[41,43] groups. However, upon evacuation (as represented in Figure 6d), mainly the MDC at 1376 and 1345 cm^{-1}[39−43] are observed along with carbonates at 1632 and 1620 cm^{-1}.[39]

Therefore, it can be inferred that the MDC formed by reactive adsorption over the Cu−I photocatalyst surfaces is quite stable in nature and is therefore retained even after evacuation. This is probably due to the fact that the Cu-1 possesses more of a Cu (1+) state or the surface O-vacancy states, which promote the formation of the MDCs. The BDC peaks are observed at 1578 and 1561 cm^{-1}[40,43,48−52] along with the bicarbonates at 1449, 1392, and 1525 cm^{-1}.[39,40] However, the carboxylates seem to be very labile in nature as they are not retained on evacuation. The −OH peak (3705 cm^{-1}) also shifts and reduces in intensity upon evacuation.[41,43]

3.3.2.2. Adsorption of CO_2 and H_2O on Cu-1 and Subsequent Evacuation. The FT-IR spectra of the Cu-1 catalyst on exposure to CO_2 and moisture simultaneously show peaks at 3586, 2746, 2356, 2120, 1689, 1668, 1637, 1587, 1513, 1484, 1424, 1407, 1349, 1323, 1282, 1256, and 1154 cm^{-1} (Figure 7). Apart from vibrational bands for surface −OH and

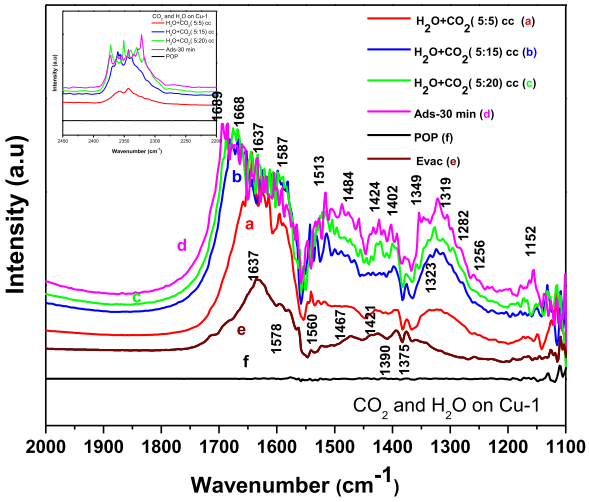

Figure 7. Adsorption of CO_2 and moisture over the Cu-1 surface; (a) 5 cm^3 H_2O and 5 cm^3 CO_2 adsorption; (b) 5 cm^3 H_2O and 15 cm^3 CO_2 adsorption; (c) 5 cm^3 H_2O and 20 cm^3 CO_2 adsorption; (d) adsorption for 30 min; (e) evacuation: 30 min; (f) pellet on pellet; the inset shows the range from 2400 to 2200 cm^{-1}.

moisture at 3583 and 2746 cm^{-1}, the peaks due to adsorbed CO_2 are also observed. Therefore, upon simultaneous adsorption of H_2O and CO_2, different pairs of surface −OH groups, as compared to that of only CO_2 adsorption, are observed. Mostly, the alteration in the vibrational frequencies signifies two different types of surface −OH groups (plausibly surface −OH possessing intramolecular H-bond or intermolecular H-bonds) with their groups or certain other −OH groups.[41,43] The most striking feature for the Cu-1 catalysts postsorption of both moisture and CO_2 is the increase in intensity of the peak at 1689 cm^{-1}, which is attributed to carboxylate,[42] which can be established by the increment in the population of the carboxylate species upon reactive adsorption. The other peaks at 1637, 1323, and 1154 cm^{-1} signify the presence of bicarbonates.[39,41,43,44,53]

The peak at 1656 cm^{-1} is assigned to a bridging carbonate. Additionally, the peaks at 1220, 1424, and 1513 cm^{-1} are

https://doi.org/10.1021/acs.chemmater.4c00748
Chem. Mater. 2025, 37, 3927−3949

assigned to bicarbonate species,[39−41,43,44,53] and the peak at 1583 cm^{-1} has been assigned to a bidentate carbonate.[39−41] The strong peak at 1281 cm^{-1} has been assigned to a bridging carbonate based on the observation of absorptions of CO_2 on Ga_2O_3. A broad small absorption at 1409 cm^{-1}, previously seen on Fe_2O_3, has been assigned to the ν_3 (OCO) mode of a bicarbonate, and the vibrational bands at 1484, 1349, 1256, and 1282 cm^{-1} are assigned to monodentate carbonates.[40,42,43,55] In general, upon the adsorption of the H_2O and CO_2, the adsorbed BDCs are transformed into carboxylates and bicarbonates, which definitely helps in the formation of CH_4 from CO_2.[39]

Upon evacuation, vibrational bands are obtained at 1637, 1578, 1560, 1467, 1421, 1390, and 1375 cm^{-1} in the bending part (Figure 7f). In the stretch region (not shown here), there are peaks at 2801 and 3550 cm^{-1}, which show the presence of different surface −OH groups over the hydrated Cu-1 surface upon reactive chemisorption of CO_2. On evacuation, the vibrational bands at 1637 and 1421 cm^{-1} (representing bicarbonates—BCs) remain intact, as compared to the adsorbed species, which show that the bicarbonates are very strongly bound intermediates. There is a shift in the vibrational band 1587 cm^{-1} to form two bands at 1578 and 1560 cm^{-1}, which are mainly due to bidentate carbonates (BDCs). It clearly shows that though these BDC species are formed, their peaks overlap within the broad bands of BC. The band at 1484 cm^{-1} shifts to 1467 cm^{-1}, which represents the surface bicarbonates. This shift signifies the transformation of weakly bound MDC to BC. The band representing the bicarbonate 1409 cm^{-1} shifts to 1390 cm^{-1}, which also represents the presence of bicarbonates. The band at 1375 cm^{-1} is also assigned for the MDCs.[49−51,55] Therefore, the different stable species after the adsorption of H_2O and CO_2 over the Cu-1 surface are mainly BC and MDC. However, in the presence of H_2O and CO_2, there is remarkable formation of the labile carboxylates. In order to understand the effect of differential electron density in the Cu states at a higher Cu concentration, the studies were extended to TiO_2 (5% Cu) (Cu-5).

3.3.3. TiO_2 (5% Cu). 3.3.3.1. Adsorption of CO_2 over the 5% Cu-Doped TiO_2 Surface and Subsequent Evacuation. The catalyst with a higher concentration of Cu in Cu-5 responds to the CO_2 adsorption as follows. FT-IR spectra of the Cu-5 catalyst (Figure 8) on exposure to CO_2 under ambient conditions reveal the presence of peaks at 1614, 1528, 1358, 1251 and 1382 cm^{-1} attributed to the BDC.[40,41,43] The peaks for the −OH groups are found at 3381 and 3180 cm^{-1}, which are not exactly the same as that on sample Cu-1. However, the intensity of the −OH peaks is quite low as compared to that of Cu-1. Again, the peaks at 1674 and 1224 cm^{-1} show the presence of bicarbonates.[39−41,43,44,53] The peak present at 1323 cm^{-1} confirms the presence of MDC-like species.[41−43] However, there is a complete absence of carboxylate-like species in this case. The peak at 1614 cm^{-1}, representing BDC, shifts to 1590 cm^{-1} with a concomitant increase in intensity as a function of time. The other peak at 1427 cm^{-1} shifts to 1417 cm^{-1}, and it becomes sharper and higher in intensity. These observations indicate the formation of the BDCs. The shoulder 1323 cm^{-1} representing the MDCs shifts to 1346 cm^{-1}, which represents their transformation to BDCs. Therefore, the MDCs are converted to BDCs over time over the Cu-5 surface. Upon evacuation, the Cu-5 catalysts show bands at 1558 and 1358 cm^{-1}, which are mainly dominated by the BDC. However, peaks pertaining to MDC were also present after evacuation at 1474 cm^{-1} and bicarbonates at 1417 and 1224 cm^{-1}.[39−41,43,44,53]

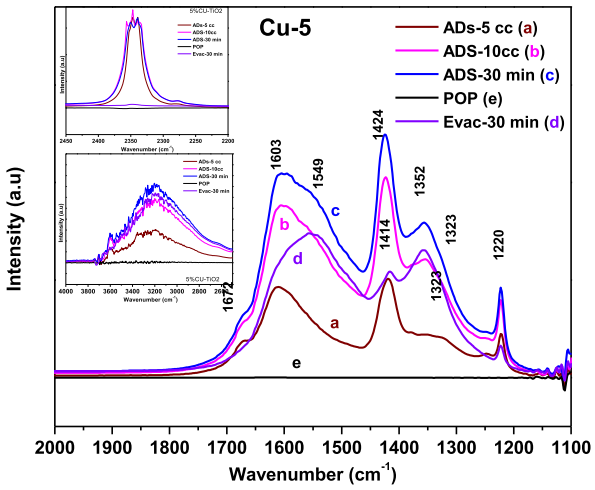

Figure 8. Adsorption of CO_2 over the Cu-5 surface (2000−1100 cm^{-1}); the inset shows the adsorbed CO_2 (2400−2200 cm^{-1}), and the other inset shows the vibrational bands from 4000 to 2400 cm^{-1} of (a) 5 cm^3 CO_2 adsorption; (b) 10 cm^3 CO_2 adsorption; (c) adsorption: 30 min; (d) evacuation: 30 min; and (e) pellet on pellet (POP).

3.3.3.2. Adsorption and Evacuation of CO_2 and H_2O over the 5% Cu-Doped TiO_2 Surface. The FT-IR spectra of the Cu-5 sample after exposure to CO_2 and moisture are given in Figure 9. There is a large shift in the stretching frequency region for the −OH group (not shown here), which shifts from 3023 and 2845 cm^{-1} to 3525 and 2855 cm^{-1}, respectively. There is also a substantial increase in the intensity and broadness of the peak. The main vibrational bands observed are at 1689, 1601, 1558, 1533, 1498, 1478, 1414, 1391, 1374, 1355, 1369, 1271, and 1220 cm^{-1}. The main peak observed after only the adsorption of moisture is at 1639 cm^{-1}, which is due to the bending modes of −OH. Mostly, it leads to different types of −OH species over the adsorption of the moisture along with CO_2. In the bending region of these bands, the peaks at 1375 and 1601 cm^{-1} are represented as BDCs. The peak at 1689 cm^{-1} represents mainly the carboxylates as depicted earlier in the Cu-1 surface; the peaks present at 1638 cm^{-1} along with a strong peak at 1558 and others at 1456 and 1414 cm^{-1} show the presence of bicarbonates.[39−41,43]

The peaks found at 1478 and 1355 cm^{-1} confirm the presence of MDC[43] over the Cu-5 surface. Also, the peaks at 1391, 1271, and 1220 cm^{-1} represent the bicarbonates—BCs, as shown earlier. However, it will be very pertinent to mention here that even with the adsorption of the moisture and CO_2, there is the formation of the carboxylate species by the reactive adsorption of CO_2 and moisture over the Cu-5 surface. However, the monodentate carbonates (MDCs) present are also scanty and are lower in population (intensity). Mostly these BDCs and MDCs are converted to form bicarbonates and carboxylates, respectively.

However, after exposure of CO_2 and moisture together, even upon evacuation, a few broad peaks were observed at 1689, 1601, 1624, 1543, 1414, and 1355 cm^{-1} (Figure 9e), confirming the presence of BC and carboxylates as a strongly adsorbed species.[39,40] The intensity of the hydroxyl bands in the stretching region is quite strong, sharper, and shifts to 2857 cm^{-1}, denoting the different set of chemisorbed species in this as compared to that from Cu-1 with only CO_2 exposure. However, in the bending region, the peaks at 1601, 1543, 1369, and 1297 cm^{-1} signify the presence of bidentate carbonates predominant even

https://doi.org/10.1021/acs.chemmater.4c00748
Chem. Mater. 2025, 37, 3927−3949

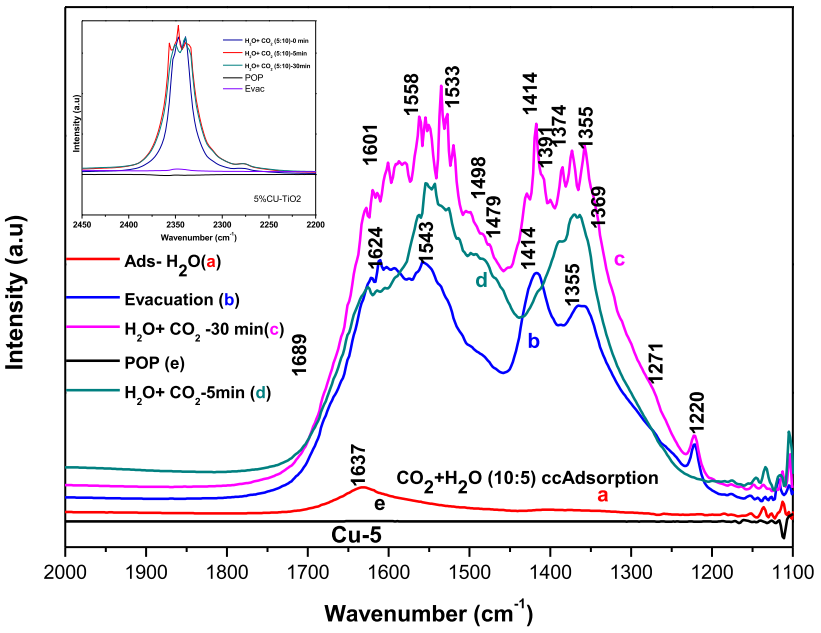

Figure 9. Adsorption of CO_2 and moisture (2000−1100 cm^{-1}) over the Cu-5 surface; (a) 5 cm^3 H_2O adsorption; (b) evacuation after adsorption for 30 min; (c) H_2O + CO_2 adsorption (5:10) cc adsorption for 30 min; (d) H_2O + CO_2 adsorption (5:10) cc-5 min; (e) pellet on pellet (POP); the inset shows vibrational bands for CO_2 (2450−2200 cm^{-1}).

after the evacuation. The peak at 1689 cm^{-1} shows the presence of carboxylates, and surprisingly, they are quite stable after exposure to CO_2 and moisture over the Cu-1 sample (still present after evacuation) as compared to that of only CO_2 exposure, which formed carboxylates labile in nature. The bands at 1414, 1355, and 1474 cm^{-1} confirm the presence of small amounts of MDCs over this surface, which are primarily formed over the electron-rich sites on the surface. Thereby, after evacuation, the presence of MDCs, BCs, and other carboxylates is ascertained.

3.3.4. TiO_2 (10% Cu). 3.3.4.1. Adsorption of CO_2 over Cu-10. The Cu-10 photocatalysts, upon exposure to CO_2 under ambient conditions, produce different reactive species as a function of time, which are depicted in Figure 10. Initially, the vibrational bands are obtained at 1618, 1419, 1340, and 1220 cm^{-1}. Later, as a function of time, different adsorption bands at 1598, 1578, 1534, 1520, 1485, 1393, and 1370 cm^{-1} are obtained. The peaks in the stretching frequency region are observed at 3180 and 3462 cm^{-1} (Figure 10A). They are quite prominent and increase as a function of time with negative bands at 3719 cm^{-1} showing the −OH over the Cu species, resulting in the adsorption of the CO_2 species.

The inset shows (Figure 10B) that the CO_2-adsorbed region contains the absorption for gas phase CO_2 at 2349 cm^{-1}, along with an additional adsorption at 2331 cm^{-1}, which has a strong shoulder at 2380 cm^{-1}. The reactive adsorption over the Cu-10 catalysts leads to the formation of mainly species pertaining to BDC represented by the dominating peaks present at 1598, 1534, 1578, 1520, and 1370 cm^{-1}.[40,41,43] The observation of a peak at 1340 cm^{-1} is ascribed to the MDC, and peaks present at 1414, 1485, and 1220 cm^{-1} show the presence of bicarbonates (BCs).[39] The band at 1618 cm^{-1} also corresponds to a bicarbonate. The primary peaks at 1542 and 1363 cm^{-1} grow as a function of time, with a slight red shift of around 4 cm^{-1}. However, in this case, there is a complete absence of carboxylates with reactive CO_2 adsorption on this catalyst surface.

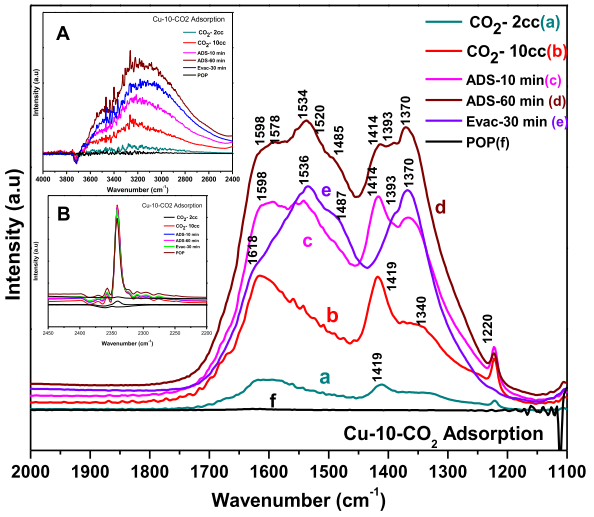

Figure 10. (A) Inset shows vibrational bands (4000−2400 cm^{-1}); (B) inset shows the adsorbed CO_2 (2450−2200 cm^{-1}) and adsorption of CO_2 over the Cu-10 surface (2000−1100 cm^{-1}) for (a) CO_2 of 2 cm^3 over the Cu-10 surface; (b) CO_2 of 10 cm^3 over the Cu-10 surface; (c) adsorption of 10 cc CO_2 over Cu-10 for 10 min; (d) adsorption of 10 cc CO_2 over Cu-10 for 60 min; (e) evacuation after adsorption for 30 min; (f) pellet on pellet (POP). (A) Inset shows adsorption of CO_2 over the Cu-10 surface (4000−2400 cm^{-1}).

However, evacuation leads to peaks at 1537, 1393, and 1373 cm^{-1} with a shoulder at 1480 and 1310 cm^{-1} (Figure 10e). The bands at 1534 and 1370 cm^{-1} show a strong presence of bidentate carbonates (BDCs), and peaks at 1487 and 1220 cm^{-1} show the presence of bicarbonates (BCs). Thereafter, the bands with very prominent intensities mainly correspond to BDCs and, surprisingly, BCs even after evacuation. There is a considerable shift in certain peaks at 1618, 1598, and 1414 cm^{-1} disappearing after evacuation. The bands at 1414 and 1618 cm^{-1} mainly represent the BCs; therefore, it is quite evident that there are two types of BCs, namely, labile and strongly adsorbed ones, over the

https://doi.org/10.1021/acs.chemmater.4c00748
Chem. Mater. 2025, 37, 3927−3949

Cu-10 catalyst. Surprisingly, some BDCs also show a labile nature at 1598 cm^{-1}.

3.3.4.2. Adsorption of CO_2 and H_2O over Cu-10. The FT-IR spectra of the Cu-10 catalyst on being exposed to CO_2 and moisture show different strong peaks at 1607, 1541, 1498, 1365, 1278, and 1220 cm^{-1} (Figure 11). An additional peak was

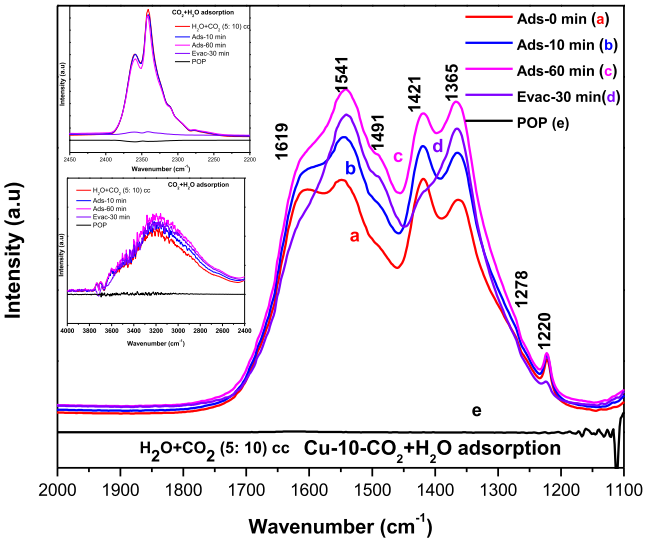

Figure 11. (A) Inset shows vibrational bands (4000−2400 cm^{-1}); (B) inset shows the adsorbed CO_2 (2450−2200 cm^{-1}) and adsorption of CO_2 and H_2O (H_2O 5 cc and CO_2 10 cc) over the Cu-10 surface (2000−1100 cm^{-1}) for (a) adsorption after 0 min over the Cu-10 surface; (b) 10 min over the Cu-10 surface; (c) 60 min over the Cu-10 surface; (d) evacuation after adsorption for 30 min; and (e) pellet on pellet (POP).

observed at 1498 cm^{-1}, which is attributed to monodentate carbonates (MDCs). Vibrational bands at 1607, 1420, and 1223 cm^{-1} are mainly assigned to bicarbonates (BCs), and the band at 1541 cm^{-1} is assigned to BDCs. The major peaks of BCs with greater intensity show that some of the BDC species have been converted to BC on exposure to CO_2 with moisture over the Cu-10 surface. Upon evacuation (Figure 11e), the major peaks are found at 1540 and 1367 cm^{-1}, representing BDCs, whereas a much less intense peak at 1223 cm^{-1} shows BC, which is present in a lower amount. Surprisingly, there is a complete absence of carboxylates with the presence of the moisture and CO_2 together that were observed for the Cu-5 and Cu-1 systems, even after the adsorption of both moisture and CO_2 on this catalyst surface along with a very small amount of bicarbonates.

In order to better understand the effect of Cu^{1+} for the formation of different intermediates upon reactive adsorption of CO_2 and H_2O over different catalytic surfaces, some of these catalysts are reduced in situ and then are exposed to CO_2 and moisture together.

3.4. In Situ Reduction of Photocatalysts Followed by Sorption of Moisture and CO_2. These photocatalysts Cu-1, Cu-10, and nano-TiO_2 were reduced in situ (in the FT-IR chamber) by using an Ar−H_2 mixture. These reduced catalysts were then exposed to CO_2 and moisture to understand the effect of the reduced Cu (Cu^{1+}) state on the different intermediates formed by reactive adsorption. The reduced nano-TiO_2 does not possess any Cu^{1+}, and hence, the effect of any reduced Ti^{4+} (Ti^{3+}/O vacancies) will be more prevalent. As the reduction potential of Cu^{2+} to Cu^{1+} is lower as compared to that of Ti^{4+} to Ti^{3+},[56] it is expected that in Cu-1 and Cu-10, more Cu^{1+} states will be produced, which will affect the formation of the intermediates.

3.4.1. Adsorption of CO_2 and H_2O over the Reduced Cu-1 Surface. The FT-IR spectra of the reduced Cu-1 catalyst upon exposure to H_2O and CO_2 as portrayed in Figure 12c show

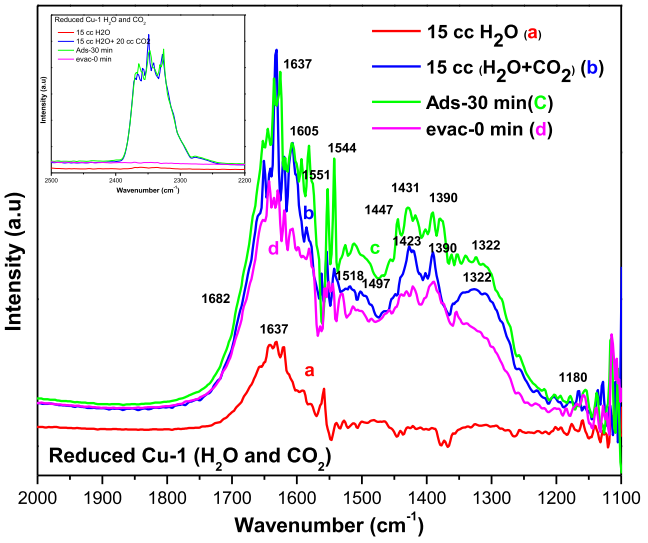

Figure 12. Adsorption of CO_2 and H_2O (H_2O-15 cc and CO_2-15 cc) over the reduced Cu-1 surface (2000−1100 cm^{-1}); the inset shows the adsorbed CO_2 (2450−2200 cm^{-1}) for (a) adsorption after 15 cc of H_2O over the reduced Cu-1 surface; (b) adsorption after 15 cc of H_2O and 20 cc CO_2 0 min; (c) adsorption for 30 min; and (d) evacuation after adsorption for 0 min.

mainly the vibrational peaks in the bending region of 2000−1100 cm^{-1} where the peaks are obtained at 1682, 1637, 1605, 1551, 1525, 1518, 1447, 1431, 1423, 1390, 1322, and 1180 cm^{-1}. Initially, upon H_2O adsorption, the major peak observed is at 1637 cm^{-1}, which is for the bending mode of the surface −OH group. As indexed previously, the bands at 1682 and 1180 cm^{-1} are assigned for carboxylate ions; 1605, 1554, 1544, 1447, 1431, and 1423 cm^{-1} are assigned for bicarbonates (BCs); and the vibrational bands obtained at 1390 and 1322 cm^{-1} are designated for the monodentate carbonates (MDCs).

It is surprising to observe that after evacuation, only the bands that disappeared are 1447, 1322, 1390, 1551, and 1637 cm^{-1} (representing BCs); however, other bands persist even after evacuation. This shows that these bicarbonates are quite labile in nature, although another very significant observation is the presence of carboxylate peaks even after evacuation. This shows that they are very stable ones after the reduction of the Cu-1 sample. This majorly indicates that upon reduction of Cu-1, the carboxylate species are stabilized mostly due to more presence of the Cu^{1+} state. Therefore, upon reduction of Cu-1, the different species that are obtained over the catalytic surface are (i) stabilized carboxylate; (ii) two types of BCs—(a) labile BC and (b) bound BC (not affected by evacuation); and (iii) stable MDCs.

3.4.2. Adsorption of CO_2 and H_2O over the Reduced Cu-10 Surface. The FT-IR spectra over the reduced Cu-10 catalyst upon exposure to H_2O and CO_2 (Figure 13) show vibrational peaks at 1609, 1538, 1487, 1421, 1371, 1299, and 1069 cm^{-1} in the bending region 2000−1100 cm^{-1}. Interestingly, there is almost no alteration in the vibrational bands for the different

https://doi.org/10.1021/acs.chemmater.4c00748
Chem. Mater. 2025, 37, 3927−3949

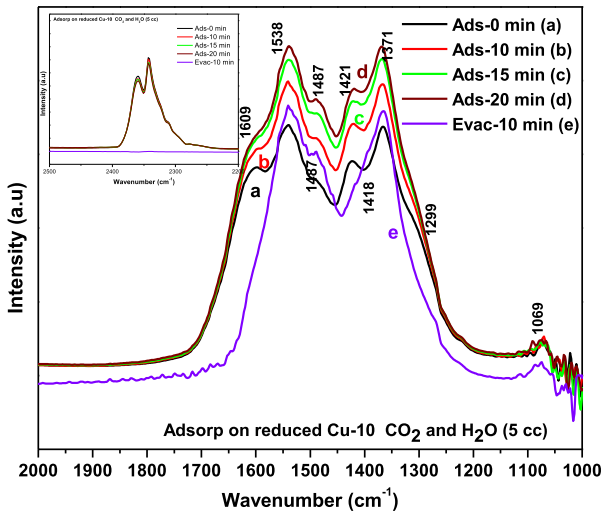

Figure 13. Adsorption of CO_2 and H_2O (H_2O 15 cc and CO_2 15 cc) over the reduced Cu-10 surface (2000−1100 cm^{-1}); the inset shows the adsorbed CO_2 (2450−2200 cm^{-1}) for adsorption after (a) 0 min; (b) 10 min; (c) 15 min; (d) 20 min; and (e) evacuation after adsorption for 10 min.

species that are obtained after the reactive adsorption of CO_2 and moisture over the Cu-10 surface before and after the reduction of Cu-10, except for an additional peak at 1299 cm^{-1}.

As understood earlier from the assignment of different vibrational bands, the bands at 1609, 1421, and 1487 cm^{-1} represent bicarbonates, 1538 cm^{-1} represents BDC, 1371 cm^{-1} represents MDC, and the peak at 1299 cm^{-1} is mainly assigned for the bridging carbonates.[54] Postevacuation, the major bands are present at 1538, 1487, 1418, and 1371 cm^{-1}. The initial band at 1538 cm^{-1} represents BDC, and others mainly BC. Therefore, in this case, both labile and bound BC species are present.

3.4.3. Adsorption of CO_2 and H_2O over the Reduced Nano-TiO_2 Surface. The FT-IR spectra of the reduced nano-TiO_2 catalyst upon exposure to H_2O and CO_2 (Figure 14) show

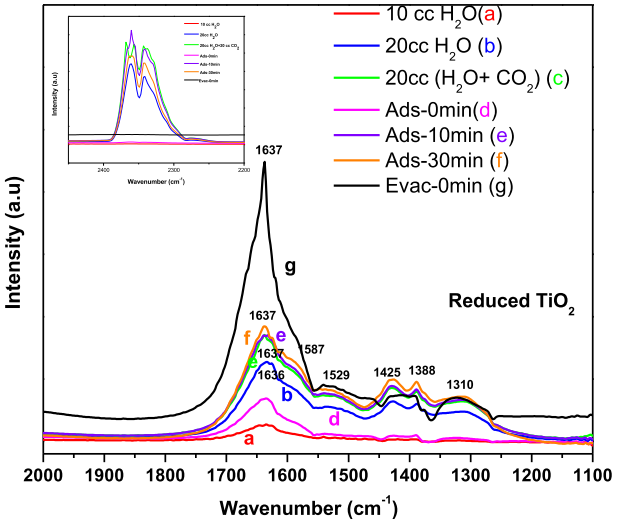

Figure 14. Adsorption of CO_2 and H_2O (H_2O 15 cc and CO_2 15 cc) over the reduced nano-TiO_2 surface (2000−1100 cm^{-1}); the inset shows the adsorbed CO_2 (2450−2200 cm^{-1}) for (a) 10 cc H_2O; (b) 20 cc H_2O; (c) adsorption of H_2O 20 cc and CO_2 20 cc; (d) 0 min; (e) 10 min; (f) 30 min; and (g) evacuation after adsorption for 0 min.

different vibrational bands present at 1637, 1587, 1529, 1425, 1388, and 1310 cm^{-1}. The major sharp peak at 1637 cm^{-1} represents the bending mode of surface −OH and that of the bridging bicarbonates as well.[44]

Initially, upon adsorption of only H_2O, it is quite understandable to assign 1637 cm^{-1} to only bending −OH. However, the sharp increase in the band upon adsorption of CO_2 points toward the formation of bridging bicarbonates as described previously in the literature.[54] The total intensity of this becomes very high due to the summation of the two peaks almost at the same place. The bands at 1587 and 1310 cm^{-1} are assigned for BDCs, 1385 cm^{-1} for MDC, and the others 1529 and 1425 cm^{-1} for the BCs. Postevacuation shows mainly bands at 1637 cm^{-1}, which is a sharp, strong band, as well as the others at 1587 cm^{-1} as a shoulder along with the bands at 1529, 1425, 1388, and 1310 cm^{-1} (Figure 14f) with the intensity of the band at 1388 cm^{-1} lowering down considerably. The surface −OH is mostly labile species, as observed for all the catalysts. Therefore, mostly, the strong band will be attributed to the adsorbed bicarbonate, which may be mostly formed due to a reduction in the nano-TiO_2 and thereby able to either dissociate the H_2O to H as a source of H for the bicarbonates from the adsorbed H_2O, leading to very stable bicarbonates over the nano-TiO_2 catalyst. The MDCs are (band at 1388 cm^{-1}) labile in nature. In order to understand the alteration of the electronic density and change in the bond order as well as the co-ordination number upon adsorption of CO_2 and moisture over different catalysts, in situ XAS studies were undertaken.

3.5. In Situ X-ray Absorption Spectroscopy (XAS) Studies during Adsorption of CO_2 and Water Vapor. The in situ XAS studies were done over the two samples Cu-5 and Cu-10 as the Cu-1 sample did not possess enough Cu to have requisite signals for the XAS studies. Therefore, Cu-5 is taken as the representative sample with a larger amount of Cu^{1+}/Cu^{2+} and a reasonable amount of surface O vacancies, as has been confirmed by the XPS studies (Figure S4), whereas the Cu-10 sample possesses only Cu^{2+} and the least amount of surface O vacancies. This has been proven by the structural study of the XANES for Cu-5 and Cu-10 also, as shown in Figure 15. With the normalized signal of the Cu-XANES signal, it is quite clear that Cu-5 possesses lower binding energy as compared to that of

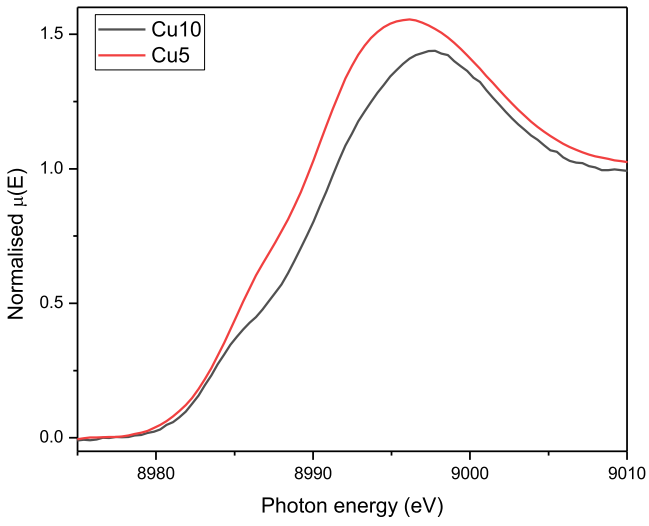

Figure 15. XANES spectra measured at the Cu K-edge for the samples Cu-5 and Cu-10.

https://doi.org/10.1021/acs.chemmater.4c00748
Chem. Mater. 2025, 37, 3927−3949

Cu-10. As there are two oxidation states of doped Cu in the TiO_2 system, namely, Cu^{1+} and Cu^{2+}, and as a function of Cu doping, the concentration of Cu^{1+} decreases, which has been amicably proven earlier in the XPS studies.[36] Therefore, the lower binding energy of Cu in Cu-5 shows the presence of some amount of Cu^{1+} in Cu-5 compared to that of Cu-10. This is more prevalent in the XPS and AES studies (Figures S3 and S4), which effectively show Cu-5 will possess more Cu^{1+} states as compared to Cu-10 (Figure S4 and Table S3).

Figure 16a,b shows the in situ XANES spectra measured at the Ti K-edge during the adsorption of CO_2 and water vapor on the

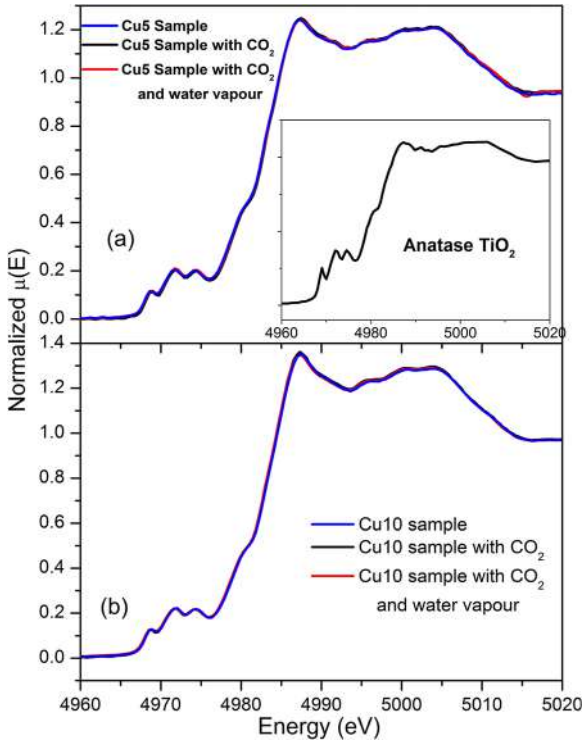

Figure 16. (a) In situ XANES spectra measured at the Ti K-edge during the adsorption of CO_2 and water vapor on the Cu5 catalyst sample. Inset: the Ti K-edge XANES spectrum of anatase TiO_2. (b) In situ XANES spectra measured at the Ti K-edge during the adsorption of CO_2 and water vapor on the Cu10 catalyst sample.

Cu5 and Cu10 catalyst samples, respectively. From the figure, it is evident that there is no significant change in the Ti K-edge XANES spectra during the adsorption of CO_2 and water vapor on Cu-doped TiO_2 catalyst samples. The XANES features of both the samples match with that of anatase TiO_2 (shown in the inset of Figure 16a). The Cu-doped TiO_2 samples at the Ti K-edge have been fitted with theoretically simulated $\chi(r)$ versus r plots generated assuming an anatase TiO_2 structure. The structural parameters for the anatase TiO_2 structure are obtained from the reported values in the literature.[14]

The EXAFS spectra have been extracted using the standard procedure.[11−13,55−57] The $\chi(k)$ spectra weighted by k^2 and the functions $\chi(k)$ and k^2 are Fourier transformed in the k range 2−10 $Å^{-1}$ to generate the $\chi(r)$ versus r (or FT-EXAFS) plots and the experimental $\chi(r)$ versus r plots. Following this structure, the experimental data have been fitted from 1 to 3.7 Å, assuming one Ti−O shell at 1.97(6×) Å and two Ti−Ti shells at 3.04(4×) and 3.79(4×) Å. The experimental $\chi(r)$ versus r plots of the Cu-5 and Cu-10 samples at the Ti K-edge along with the best-fit theoretical plots carried out as above are shown in Figure 17a,b, respectively, and the fitting results are tabulated in Table 2.

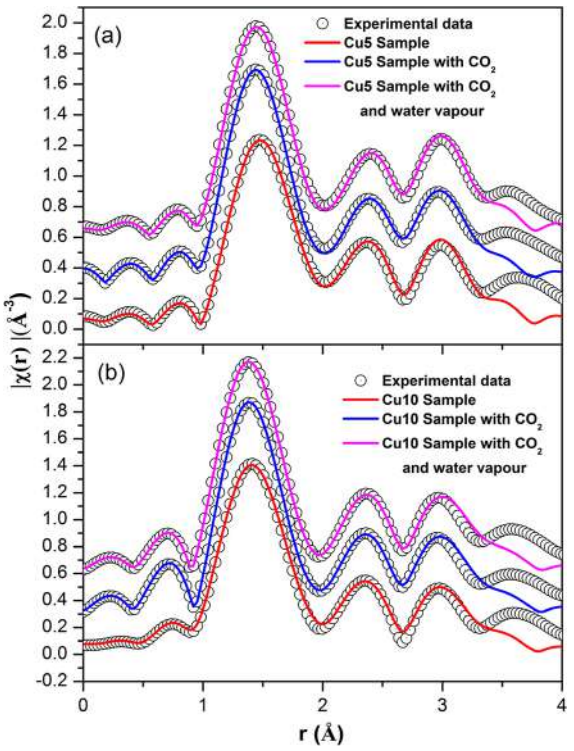

Figure 17. (a) In situ EXAFS spectra measured at the Ti K-edge during the adsorption of CO_2 and water vapor on the Cu5 catalyst sample. (b) In situ EXAFS spectra measured at the Ti K-edge during the adsorption of CO_2 and water vapor on the Cu10 catalyst sample. Open circles: experimental data and solid lines: best theoretical fit.

From the EXAFS analysis results at the Ti K-edge (Table 2), it is evident that the variation of the Ti−Ti bond lengths and coordination numbers is within the error bars. However, the Ti−O bond length decreases with the adsorption of CO_2 and water vapor for both samples. For both the as-prepared samples, the Ti−O coordination number values are less than the theoretical values of the anatase TiO_2 structure (i.e., 6). This suggests the presence of oxygen vacancies in the TiO_2 lattice near the Ti cations. The Ti−O coordination increases on adsorption of CO_2 and decreases on adsorption of water vapor. Therefore, from the XANES and EXAFS analyses at the Ti K-edge, it can be inferred that the effective charge of Ti cations does not change during the adsorption of CO_2 and water vapor. However, the Ti−O bond lengths and coordination numbers change, which suggests that the oxygen vacancies near the Ti sites participate in the adsorption process. The oxygen vacancies decrease on adsorption of CO_2, and it again increases on adsorption of water vapor.

Figure 18a,b shows the in situ XANES spectra measured at the Cu K-edge during the adsorption of CO_2 and water vapor on the Cu5 and Cu10 catalyst samples, respectively. The inset in both Figure 5a,b gives an enlarged view of the absorption edge. It has been found from the spectra that the effective charge of Cu in the samples increases during CO_2 adsorption and decreases during H_2O adsorption (Tables S4 and S5). This suggests that Cu cations play an important role in both CO_2 and H_2O adsorption.

The EXAFS spectra have been extracted using the standard procedure.[11−13,43,53,56] The $\chi(k)$ spectra is weighted by k^2, and

https://doi.org/10.1021/acs.chemmater.4c00748
Chem. Mater. 2025, 37, 3927−3949

Table 2. Ti K-Edge EXAFS Fitting of Cu-Doped TiO_2 Samples during Adsorption of CO_2 and Water Vapor

	Ti−O1			Ti−Ti1			Ti−Ti2		
	r (Å)	N	σ^2 (Å^2)	r (Å)	N	σ^2 (Å^2)	r (Å)	N	σ^2 (Å^2)
Cu5	1.94 ± 0.01	5.5 ± 0.2	0.0061 ± 0.0011	2.94 ± 0.02	4.1 ± 0.4	0.0109 ± 0.0020	3.69 ± 0.02	3.4 ± 0.5	0.0026 ± 0.0023
Cu5 + CO_2	1.92 ± 0.01	5.9 ± 0.2	0.0049 ± 0.0010	2.93 ± 0.01	4.4 ± 0.5	0.0086 ± 0.0018	3.71 ± 0.02	3.4 ± 0.5	0.0022 ± 0.0021
Cu5 + (CO_2 and H_2O)	1.90 ± 0.01	5.6 ± 0.1	0.0043 ± 0.0007	2.92 ± 0.01	4.2 ± 0.3	0.0076 ± 0.0012	3.71 ± 0.01	3.4 ± 0.3	0.0012 ± 0.0011
Cu10	1.97 ± 0.04	5.4 ± 0.2	0.0052 ± 0.0015	2.96 ± 0.02	4.2 ± 0.5	0.0050 ± 0.0027	3.74 ± 0.02	4.1 ± 0.6	0.0036 ± 0.0030
Cu10 + CO_2	1.94 ± 0.01	5.8 ± 0.1	0.0043 ± 0.0010	2.96 ± 0.01	4.1 ± 0.4	0.0075 ± 0.0019	3.75 ± 0.02	4.3 ± 0.5	0.0034 ± 0.0021
Cu10 + (CO_2 + H_2O)	1.94 ± 0.01	5.6 ± 0.1	0.0041 ± 0.0012	2.97 ± 0.02	4.2 ± 0.4	0.0085 ± 0.0024	3.76 ± 0.02	3.8 ± 0.7	0.0019 ± 0.0014

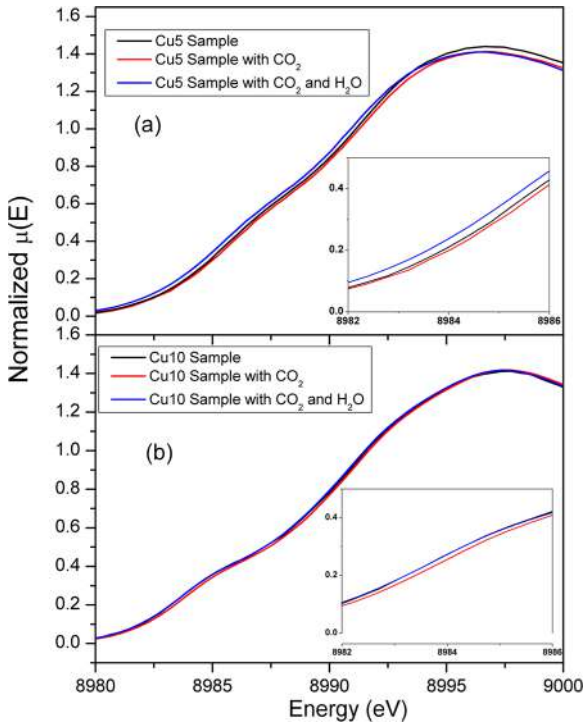

Figure 18. (a) In situ XANES spectra measured at the Cu K-edge during the adsorption of CO_2 and water vapor on the Cu5 catalyst sample. Inset: an enlarged view of the absorption edge. (b) In situ XANES spectra measured at the Cu K-edge during the adsorption of CO_2 and water vapor on the Cu10 catalyst sample. Inset: an enlarged view of the absorption edge.

the functions $\chi(k)k^2$ are Fourier transformed in the k range 2−10 Å^{-1} to generate the $\chi(r)$ versus r plots shown in Figure 16. It can be observed from Figure 6 that the peak at 1.4 Å corresponds to the Cu−O path; however, the features between 2 and 3 Å are due to contributions from higher coordination shells. These features vary significantly for both Cu5 and Cu10 samples on adsorption of CO_2 and water vapor but could not be fitted with any structural model due to the broadness of the peaks.

The significant variations of the EXAFS features in Figure 18 suggest that the local environment around the Cu cations changes during the adsorption of CO_2 and water vapor. The experimental $\chi(r)$ versus r plots of the Cu-doped TiO_2 samples at the Cu K-edge have been fitted from 1 to 2 Å with a Cu−O shell at 1.97(6×) Å, assuming Cu replaces Ti in the anatase TiO_2 structure.[4,60] The experimental $\chi(r)$ versus r plots of the Cu-5 and Cu-10 samples at the Cu K-edge along with the best-fit theoretical plots carried out as above are shown in Figure 19a,b, respectively, and the fitting results are tabulated in Table 3.

From the EXAFS analysis results, it can be inferred that the Cu−O coordination number partially decreases on adsorption of CO_2 and water vapor for both the samples. This implies the creation of oxygen vacancies near Cu cations due to both adsorptions of CO_2 and water vapor. It should also be noted that the Cu−O bond length does not vary significantly for the Cu-5 sample during adsorption of CO_2 and water vapor, though for the Cu-10 sample the Cu−O bond length increases on adsorption of CO_2 and water vapor. From the XANES and EXAFS analysis, it is evident that the effective charge and local environment of Cu cations change significantly upon adsorption of CO_2 and water vapor, which indicates the participation of Cu cations in the adsorption process.

https://doi.org/10.1021/acs.chemmater.4c00748
Chem. Mater. 2025, 37, 3927−3949

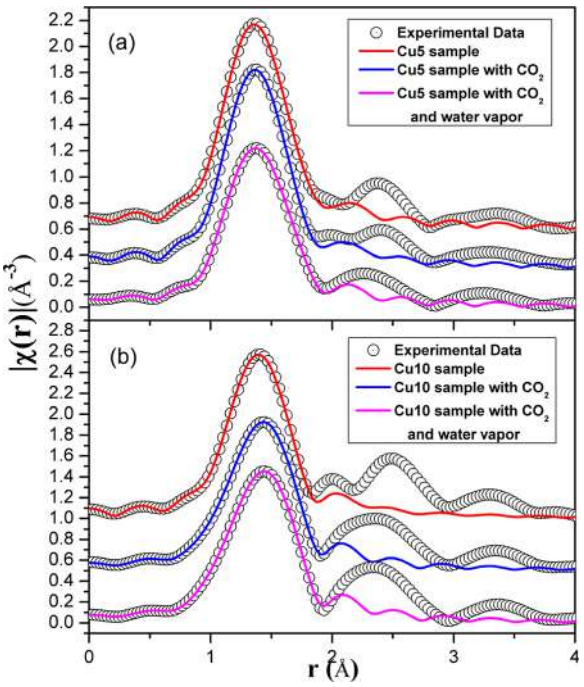

Figure 19. In situ EXAFS spectra measured at the Cu K-edge during the adsorption of CO_2 and water vapor on the Cu5 catalyst sample. (b) In situ EXAFS spectra measured at the Cu K-edge during the adsorption of CO_2 and water vapor on the Cu10 catalyst sample. Open circles: experimental data and solid lines: best theoretical fit.

Table 3. Cu K-Edge EXAFS Fitting of Cu-Doped TiO_2 Samples during Adsorption of CO_2 and Water Vapor

	Cu−O		
	r (Å)	N	σ^2 (Å^2)
Cu5	1.92 ± 0.03	5.2 ± 0.2	0.0044 ± 0.0023
Cu5 with CO_2	1.91 ± 0.03	4.8 ± 0.1	0.0036 ± 0.0015
Cu5 with CO_2 and water vapor	1.92 ± 0.02	4.7 ± 0.2	0.0057 ± 0.0008
Cu10	1.91 ± 0.01	5.0 ± 0.3	0.0036 ± 0.0008
Cu10 with CO_2	1.93 ± 0.01	4.6 ± 0.2	0.0039 ± 0.0021
Cu10 with CO_2 and water vapor	1.94 ± 0.02	4.7 ± 0.2	0.0042 ± 0.0026

3.6. In Situ XAS Studies during Photocatalytic Reduction of CO_2.

Figure 20a,b shows the in situ XANES spectra measured at the Ti K-edge during the photocatalytic reduction of CO_2 with Cu5 and Cu10 catalyst samples, respectively. The insets in both the figures give an enlarged view of the pre-edge region, which shows three small peaks termed A1, A2, and A3. The peaks A1 and A2 correspond to the 3d−4p hybridized state transition, and the peak A3 corresponds to the 4p−4s transition. In anatase TiO_2, the A1 peak corresponds to the four Ti neighbors of the first Ti−Ti shell, and the peak A2 is related to the Ti neighbors of the second Ti−Ti shell. Peak A3 arises due to Ti 4p hybridization with Ti 4s and/or O 2p orbitals.[14,15,54,58] From the figure, it is evident that the Cu10 sample does not show any significant changes. However, for the Cu-5 sample, the pre-edge peaks A1, A2, and A3 increase in intensity and move toward higher energy as the reaction proceeds. The increase in the pre-edge peak intensities is often associated with distortion in the TiO_6 octahedra of anatase TiO_2, which results in higher orbital mixing between Ti and O.[16,59]

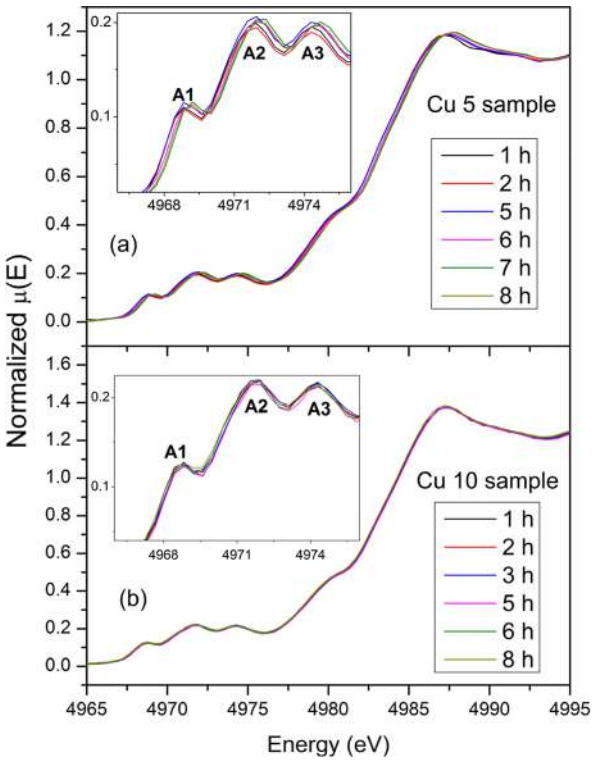

Figure 20. (a) In situ XANES spectra measured at the Ti K-edge of the Cu-5 catalyst sample during the photocatalytic reduction of CO_2. Inset: an enlarged view of pre-edge peaks. (b) In situ XANES spectra measured at the Ti K-edge of the Cu-10 catalyst sample during the photocatalytic reduction of CO_2. Inset: an enlarged view of pre-edge peaks.

The experimental $\chi(r)$ versus r plots of the Cu-5 and Cu-10 samples at the Ti K-edge along with best-fit theoretical ones are shown in Figure 21a,b, respectively, and the fitting results are tabulated in Tables 4 and 5. From the EXAFS analysis results, it is evident that the coordination numbers of the Ti−O bond increase as the reaction proceeds. However, the Ti−O and Ti−Ti bond lengths do not change significantly during the reaction. The increase in the Ti−O coordination number implies the decrease in oxygen vacancies near Ti cations, which suggests that the oxygen vacancies play a role in the photocatalytic reduction of CO_2.

Figure 22a,b shows the in situ XANES spectra measured at the Cu K-edge during the photocatalytic reduction of CO_2 with Cu-5 and Cu-10 catalyst samples, respectively. From the above figures, it can be observed that the absorption edge in general shifts toward lower energy with time during the photocatalytic reduction of CO_2 for both the catalyst samples. This implies that the effective charge of Cu decreases during the photocatalytic reduction of CO_2.

However, at certain time intervals, there is a slight increase in the Cu effective charge, as evident from the shift of the absorption edge to higher energy shown in Figure 23. The experimental $\chi(r)$ versus r plots of the Cu-5 and Cu-10 samples at the Cu K-edge along with the best-fit theoretical plots are shown in Figure 18a,b, respectively, and the fitting results are tabulated in Tables 6 and 7. From the EXAFS analysis results, it can be seen that the Cu−O bond lengths and coordination numbers do not vary significantly during the photocatalytic reduction of CO_2 for both Cu-5 and Cu-10 samples. Therefore, it can be concluded from the XANES and EXAFS analysis that

https://doi.org/10.1021/acs.chemmater.4c00748
Chem. Mater. 2025, 37, 3927−3949

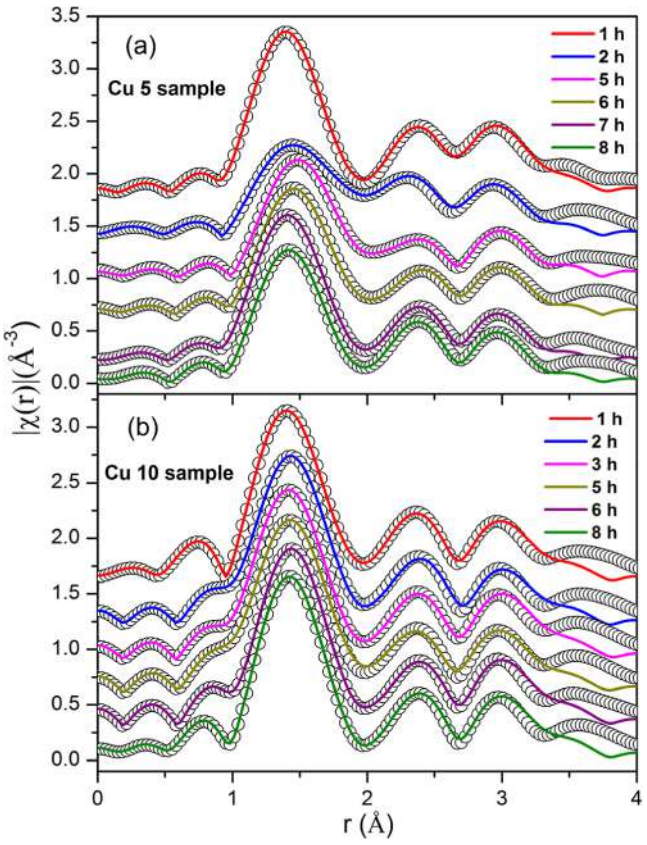

Figure 21. (a) In situ EXAFS spectra measured at the Ti K-edge of the Cu-5 catalyst sample during the photocatalytic reduction of CO_2. (b) In situ EXAFS spectra measured at the Ti K-edge of the Cu-5 catalyst sample during the photocatalytic reduction of CO_2. Rounds: experimental data and solid lines: best theoretical fit.

the effective charge of Cu was shown to decrease during the photocatalytic reduction of CO_2, but there is no change in the local environment of Cu cations.

3.6.1. Gas Chromatograph Measurements. From the gas chromatograph measurements, it has been confirmed that CH_4 is produced during the photocatalytic reduction of CO_2 (Figure S3), showing the variation of CH_4 concentration with time during the photocatalytic reduction of CO_2 as determined from the GC measurements. The methane peak appears after 2 and 3 h from the start of the reaction for 50 mg of the Cu-5 and Cu-10 samples, respectively.

3.7. Discussion. *3.7.1. Nano-TiO_2.* The synthesized nano-TiO_2 is photocatalytically inactive for the reduction of CO_2 to CH_4 as has been observed earlier.[20] The intent of observing the different intermediates over nano-TiO_2 upon exposure to CO_2 and H_2O and after reduction is mainly to understand how the anatase TiO_2 in the absence of any Cu behaves toward the adsorption process. However, being inactive, the in situ reaction for operando EXAFS was not carried over. The intermediates upon exposure to CO_2 are BDC and BC, and upon adsorption of H_2O and CO_2, it is primarily BC. It establishes that in the presence of H_2O, the BDCs are converted to BCs. The intermediates observed over reduced TiO_2 are mainly bicarbonates MDC and BDC. However, there is no formation of carboxylate under any of these conditions. The XPS studies show Ti is present as Ti^{4+} only, and there is a negligible amount of O vacancy present (Figure S2). This could be explained by Scheme 1. The geometry favors coordination of the C in CO_2 to the basic O atom site and coordination of an O in CO_2 to the strong Ti Lewis acid site. The question of which atom is coordinated first is energetically more favorable for the C atom in CO_2 to coordinate to the basic O atom site on the surface,[60] followed by coordination of a CO_2−O atom to the acidic Ti-site.

The electron density over Ti in reduced nano-TiO_2 would decrease, which would result in less back-bonding, as observed in Scheme 1A,B, leading to mainly MDCs and BCs, which are labile in nature. The presence of the BDC could be explained by the fact that there will be certain Ti^{4+} sites which will be less affected by the reduction and would follow the B route of Scheme 1 and would result in a very strongly held BDC or BC.

3.7.2. Cu-5 Catalysts. The Cu-5 catalysts upon reactive adsorption of CO_2 form mainly BDC; however, the formation of BC and MDC is also observed. Nevertheless, upon the adsorption of H_2O and CO_2, there is the formation of carboxylate and BCs and MDC, and the carboxylate and the BC are stable in nature. The XAS study shows (a) the Cu-5 has lower binding energy as compared to Cu-10, showing evidence of the presence of Cu^{1+} in Cu-5 (Figures S3 and S2). (b) XANES and EXAFS analyses at the Ti K-edge for Cu-5 indicate that the effective charge of Ti cations does not change during the adsorption of CO_2 and water vapor. However, the Ti−O bond lengths and coordination numbers change, which suggests that the oxygen vacancies near the Ti sites participate in the adsorption process. The oxygen vacancies decrease on adsorption of CO_2, and it again increases on adsorption of water vapor, and (c) in situ XANES spectra measured at the Cu K-edge during the adsorption of CO_2 and water vapor on Cu5 spectra show that the effective charge of Cu in the samples increases during CO_2 adsorption and decreases during H_2O adsorption. Therefore, it can be inferred that the Cu−O coordination number decreases on adsorption of CO_2 and water vapor for both samples. This implies the creation of oxygen vacancies near Cu cations due to both adsorptions of CO_2 and water vapor. These studies all combined together reveal that the adsorption of CO_2 and H_2O results in Cu^{1+} to form Cu^{2+}. Use of

Table 4. Ti K-Edge EXAFS Fitting of the Cu-5 Sample during the Photocatalytic Reduction of CO_2

reaction time (h)	Ti−O1			Ti−Ti1			Ti−Ti2		
	r (Å)	N	σ^2 (Å^2)	r (Å)	N	σ^2 (Å^2)	r (Å)	N	σ^2 (Å^2)
1	1.90 ± 0.01	5.3 ± 0.2	0.0028 ± 0.0007	2.94 ± 0.01	3.6 ± 0.3	0.0055 ± 0.0013	3.72 ± 0.01	3.2 ± 0.3	0.0015 ± 0.0005
2	1.91 ± 0.01	5.6 ± 0.3	0.0106 ± 0.0015	2.91 ± 0.01	3.5 ± 0.3	0.0045 ± 0.0015	3.69 ± 0.02	3.6 ± 0.5	0.0048 ± 0.0023
5	1.91 ± 0.01	5.8 ± 0.2	0.0067 ± 0.0008	2.91 ± 0.01	3.9 ± 0.3	0.0087 ± 0.0013	3.69 ± 0.01	3.9 ± 0.5	0.0070 ± 0.0020
6	1.89 ± 0.01	6.0 ± 0.4	0.0063 ± 0.0012	2.93 ± 0.01	3.9 ± 0.3	0.0088 ± 0.0015	3.72 ± 0.01	3.9 ± 0.5	0.0069 ± 0.0021
7	1.90 ± 0.01	6.1 ± 0.2	0.0052 ± 0.0011	2.93 ± 0.01	3.9 ± 0.3	0.0082 ± 0.0013	3.71 ± 0.01	3.5 ± 0.5	0.0059 ± 0.0019
8	1.91 ± 0.01	6.2 ± 0.2	0.0073 ± 0.0008	2.93 ± 0.01	3.9 ± 0.3	0.0075 ± 0.0013	3.71 ± 0.02	3.6 ± 0.5	0.0056 ± 0.0019

https://doi.org/10.1021/acs.chemmater.4c00748
Chem. Mater. 2025, 37, 3927−3949

Table 5. Ti K-Edge EXAFS Fitting of the Cu-10 Sample during the Photocatalytic Reduction of CO_2

reaction time (h)	Ti−O1			Ti−Ti1			Ti−Ti2		
	r (Å)	N	σ^2 (Å^2)	r (Å)	N	σ^2 (Å^2)	r (Å)	N	σ^2 (Å^2)
1	1.95 ± 0.01	5.4 ± 0.1	0.0038 ± 0.0009	2.97 ± 0.01	4.1 ± 0.4	0.0068 ± 0.0018	3.75 ± 0.02	4.0 ± 0.5	0.0033 ± 0.0021
2	1.96 ± 0.01	5.6 ± 0.3	0.0045 ± 0.0011	2.97 ± 0.01	4.1 ± 0.5	0.0069 ± 0.0020	3.75 ± 0.02	3.4 ± 0.6	0.0029 ± 0.0018
3	1.96 ± 0.01	5.5 ± 0.3	0.0041 ± 0.0010	2.97 ± 0.01	3.9 ± 0.4	0.0067 ± 0.0019	3.76 ± 0.02	4.2 ± 0.6	0.0029 ± 0.0020
5	1.96 ± 0.01	5.6 ± 0.3	0.0043 ± 0.0012	2.95 ± 0.02	4.1 ± 0.5	0.0069 ± 0.0023	3.73 ± 0.02	3.9 ± 0.6	0.0028 ± 0.0015
6	1.95 ± 0.01	5.7 ± 0.2	0.0042 ± 0.0009	2.96 ± 0.01	4.3 ± 0.5	0.0079 ± 0.0018	3.74 ± 0.01	3.9 ± 0.5	0.0024 ± 0.0019
8	1.95 ± 0.01	5.8 ± 0.2	0.0038 ± 0.0009	2.96 ± 0.01	4.1 ± 0.5	0.0075 ± 0.0020	3.74 ± 0.02	3.7 ± 0.5	0.0022 ± 0.0016

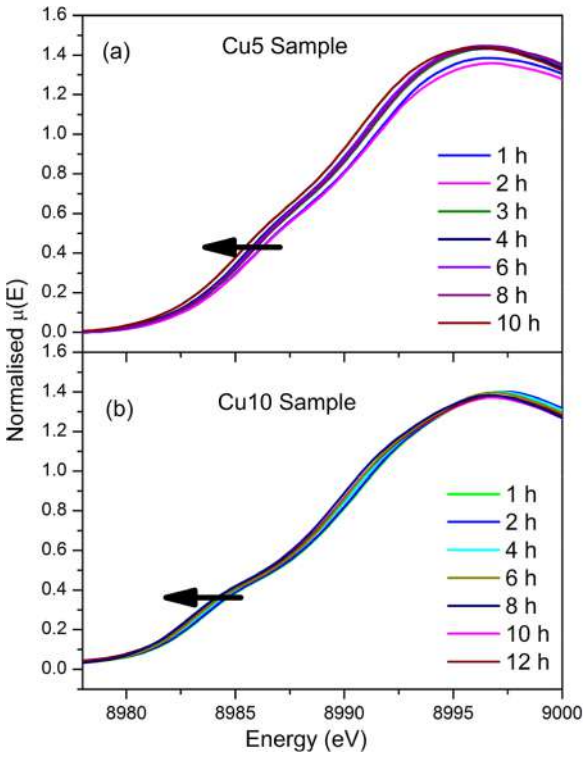

Figure 22. (a) In situ XANES spectra measured at the Cu K-edge of the Cu-5 catalyst sample during the photocatalytic reduction of CO_2. (b) In situ XANES spectra measured at the Cu K-edge of the Cu10 catalyst sample during the photocatalytic reduction of CO_2.

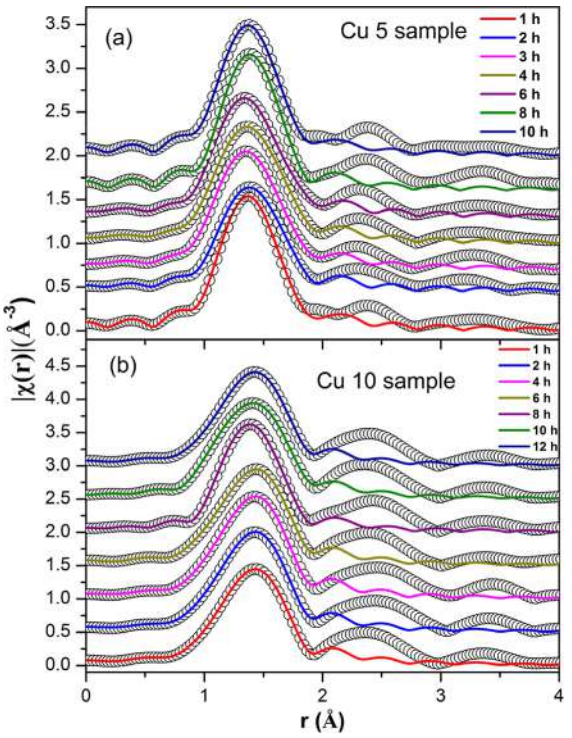

Figure 23. (a) In situ EXAFS spectra measured at the Cu K-edge of the Cu-5 catalyst sample during the photocatalytic reduction of CO_2. (b) In situ EXAFS spectra measured at the Cu K-edge of the Cu-5 catalyst sample during the photocatalytic reduction of CO_2. Open circles: experimental data and solid lines: best theoretical fit.

Cu^{1+} in the process of CO_2 adsorption and formation of Cu^{2+} and the O vacancies both near Cu and Ti participates in the process of sorption of CO_2 and H_2O. The intermediate carboxylate is formed over the electron-rich centers as upon H_2O/CO_2 adsorption, the binding energy of Cu is lowered, and at these sites, the carboxylates are formed. The above is represented in Scheme 2, which clearly shows that in the presence of the Cu^{1+} state, only the carboxylate is formed, as observed from the XANES study of Cu-5. Also, the EXAFS study shows that there is very little change in the Cu−O bond distance for Cu-5, which can also be explained from Scheme 2. The Cu−O bond length will only change if there is very strong back-bonding resulting in very stable BDCs; however, in Cu-5, there is formation of stable carboxylates, stable MDCs, and labile BCs when Cu-5 is exposed to H_2O and CO_2, which explains that there will be less change in the Cu−O bond length, but there will be some change in the co-ordination number as the O vacancies formed will be utilized for the formation of labile BC, MDC, and BC and a lower amount of BDC, which does not alter the Cu−O bond length.

Table 6. Cu K-Edge EXAFS Fitting of the Cu-5 Sample during the Photocatalytic Reduction of CO_2

reaction time (h)	Cu−O		
	r (Å)	N	σ^2 (Å^2)
1	1.92 ± 0.02	4.8 ± 0.3	0.0033 ± 0.0006
2	1.93 ± 0.02	4.7 ± 0.3	0.0059 ± 0.0011
3	1.92 ± 0.01	4.9 ± 0.4	0.0054 ± 0.0015
4	1.93 ± 0.01	4.9 ± 0.4	0.0055 ± 0.0015
6	1.92 ± 0.02	4.9 ± 0.6	0.0056 ± 0.0023
8	1.92 ± 0.01	5.0 ± 0.3	0.0031 ± 0.0014
10	1.91 ± 0.03	4.7 ± 0.5	0.0034 ± 0.0025

3.7.3. Cu-10. The reactive adsorption of CO_2 and CO_2 and H_2O over the Cu-10 catalyst shows mainly the formation of BDCs and in small amounts MDCs and BCs, where postevacuation, the most stable species are the BDCs and BCs. The exposure of H_2O and CO_2 together also forms mainly BDCs and strongly bound BCs. The reduced Cu-10 upon exposure to CO_2 and moisture shows the formation of BDCs

https://doi.org/10.1021/acs.chemmater.4c00748
Chem. Mater. 2025, 37, 3927−3949

Table 7. Cu K-Edge EXAFS Fitting of the Cu-10 Sample during the Photocatalytic Reduction of CO_2

reaction time (h)	Cu−O		
	r (Å)	N	σ^2 (Å^2)
1	1.93 ± 0.01	5.1 ± 0.7	0.0048 ± 0.0022
2	1.92 ± 0.03	5.3 ± 0.4	0.0053 ± 0.0014
3	1.92 ± 0.03	5.2 ± 0.4	0.0051 ± 0.0010
4	1.92 ± 0.03	5.4 ± 0.7	0.0054 ± 0.0005
5	1.92 ± 0.02	5.2 ± 0.4	0.0050 ± 0.0004
6	1.93 ± 0.01	5.2 ± 0.7	0.0054 ± 0.0021
7	1.92 ± 0.02	5.4 ± 0.3	0.0048 ± 0.0008
8	1.92 ± 0.02	5.2 ± 0.4	0.0037 ± 0.0013
9	1.93 ± 0.02	5.1 ± 0.8	0.0050 ± 0.0023
10	1.93 ± 0.01	5.2 ± 0.6	0.0054 ± 0.0015
11	1.93 ± 0.02	5.1 ± 0.5	0.0037 ± 0.0006
12	1.93 ± 0.01	5.0 ± 0.7	0.0051 ± 0.0017

and strongly bound BCs. The XAS studies over the Cu-10 show these prime factors: (1) the binding energy for the Cu-10 increases as compared to that of Cu-5, and the previous studies with XPS show that there is a lower amount of Cu^{1+} and surface O vacancies in Cu-10; (2) from XANES and EXAFS analyses at the Ti K-edge, it can be inferred that the effective charge of Ti cations for Cu-10 does not change during the adsorption of CO_2 and water vapor, but the Ti−O bond lengths and coordination numbers change, which suggests that the oxygen vacancies near the Ti sites participate in the adsorption process; (3) the Cu K-edge during the adsorption of CO_2 and water vapor in the Cu-10 catalyst shows an increase in the effective charge of Cu in the samples increases during CO_2 adsorption and decrease during H_2O adsorption. Local environments around the Cu cations change during the adsorption of CO_2 and water vapor, and the Cu−O coordination number decreases on adsorption of CO_2 and water vapor for both the samples. This implies the creation of oxygen vacancies near Cu cations due to both adsorptions of CO_2 and water vapor. It should also be noted that the Cu−O bond length does not vary significantly for the Cu5 sample during adsorption of CO_2 and water vapor, though for the Cu10 sample, the Cu−O bond length increases on adsorption of CO_2 and water vapor. These could be explained by these intermediates formed, as shown in Scheme 3. This would be explained by the fact that in Cu-10, most of the intermediates formed would be formed by the back-bonding to form an extra Cu−O bond, which explains the fact that the Cu−O bond length increases on adsorption of CO_2 and water vapor. Both the structural XANES study and the previous XPS studies show that there is a much smaller amount of Cu^{1+} and surface O vacancies in the Cu-10 sample. This study establishes the fact that the

Scheme 1. Intermediates Formed on Adsorption of CO_2 and CO_2 + H_2O over the Nano-TiO_2 Surface

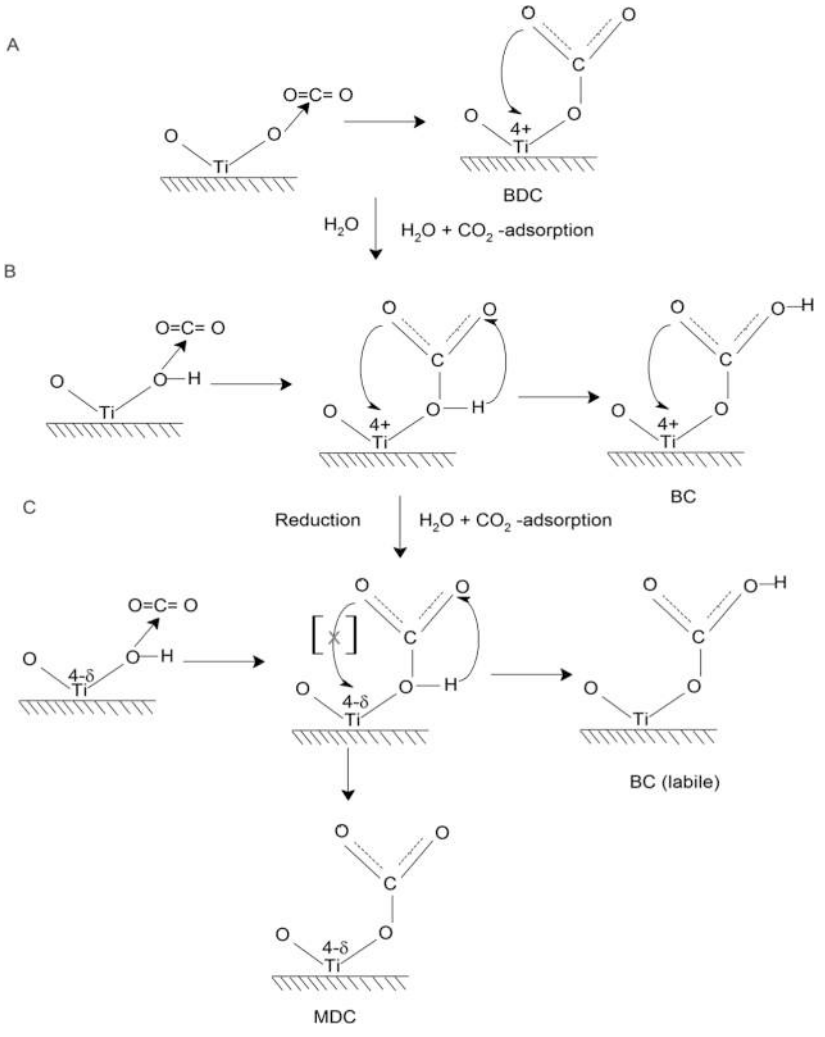

https://doi.org/10.1021/acs.chemmater.4c00748
Chem. Mater. 2025, 37, 3927−3949

Scheme 2. Intermediates Formed on Adsorption of CO_2 and CO_2 + H_2O over the Cu-5 Surface

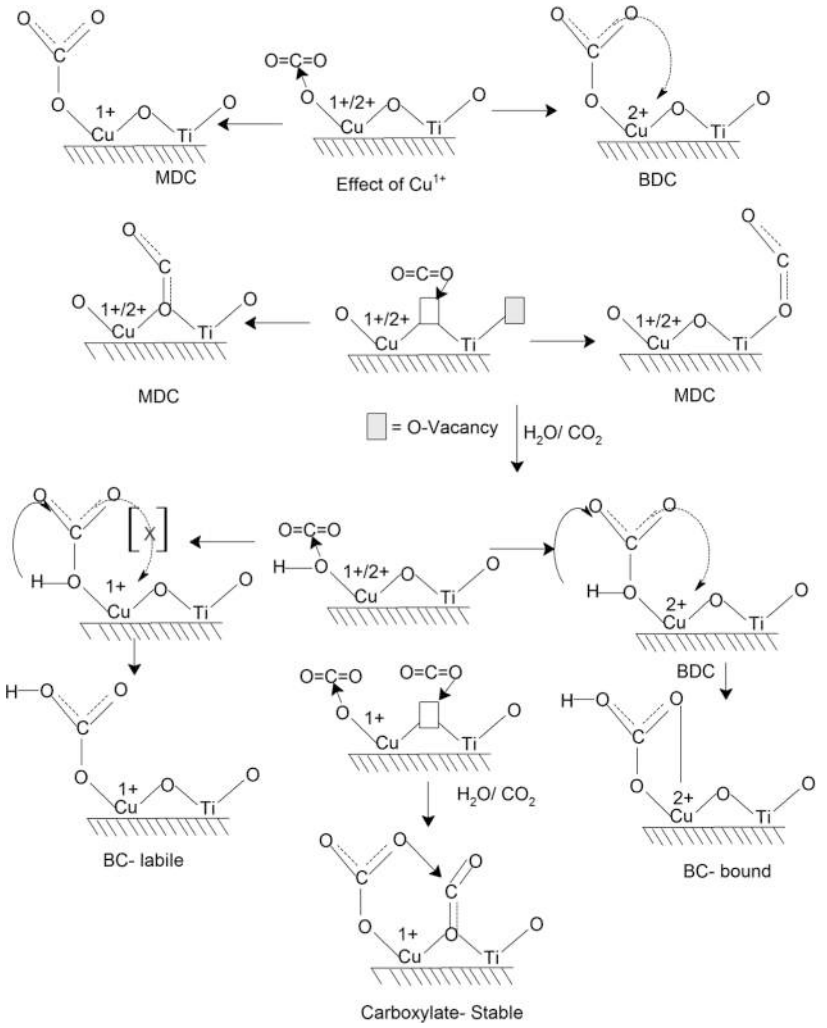

formation of the carboxylates is not observed at all, even on the reduced Cu-10 sample, which mainly shows that the formation of carboxylates, mainly Cu^{1+}, plays a role along with the surface O vacancy.

3.7.4. Cu-1. The understanding of the simplistic models for the Cu-5 and the Cu-10 systems could be rather extrapolated for the Cu-1 system as XAS data could not be collected on this sample owing to the lower concentration of Cu. The previous XPS studies have shown that in the Cu-1 system, Cu^{1+} is present in the maximum amount along with the surface O vacancies.[21] Also, as in the Cu-5 sample, which has a strong amount of Cu^{1+} and O vacancies, these will lead to the formation of a carboxylate intermediate, which should perhaps be more stable in Cu-1 due to the presence of a greater amount of Cu^{1+} and O vacancies in the vicinity. The BDCs will be formed in a smaller amount in Cu-1 along with the formation of labile and strongly bound BC with H_2O and CO_2 exposure. The different intermediates found for Cu-1 are (a) on CO_2 reactive adsorption, the carboxylates are formed along with a higher amount of MDCs and BCs; (b) upon H_2O and CO_2 exposure, the carboxylates intensity grows, and the BCs formed are both labile and strongly adsorbed. However, upon reduction, the carboxylates become stable in nature, mostly due to the fact that the reduction would enable more concentration of Cu^{1+} and O vacancies in the vicinity.

The simple model explains the formation of different intermediates formed as a function of electron density around Cu and O vacancies in the formation of the different adsorptive intermediates. For the photocatalytic reaction, the intermediates formed will be different, and the effect of Cu and the nature of different stable intermediates formed upon reactive adsorption CO_2 and H_2O needs to be explored.

3.8. In Situ XAS Studies for Photoreduction of CO_2 and Moisture and the Reaction Mechanism. The in situ XAS studies during the photocatalytic reduction of CO_2 and moisture show these salient features:

a In the Cu-5 sample, the pre-edge peaks A1, A2, and A3 increase in intensity and shift toward higher energy as the reaction proceeds; however, the Cu10 sample does not show any significant changes in the in situ XANES study.

b In situ EXAFS for the Ti K-edge shows the coordination numbers of the Ti−O bond increase as the reaction proceeds. However, the Ti−O and Ti−Ti bond lengths do not change significantly during the reaction.

c Cu K-edge during the photocatalytic reduction of CO_2 with Cu-5 and Cu-10 shows that the absorption edge in general shifts toward lower energy with time during the photocatalytic reduction of CO_2 for both the catalyst samples.

https://doi.org/10.1021/acs.chemmater.4c00748
Chem. Mater. 2025, 37, 3927−3949

Scheme 3. Intermediates Formed on Adsorption of CO_2 and CO_2 + H_2O over the Cu-10 Surface

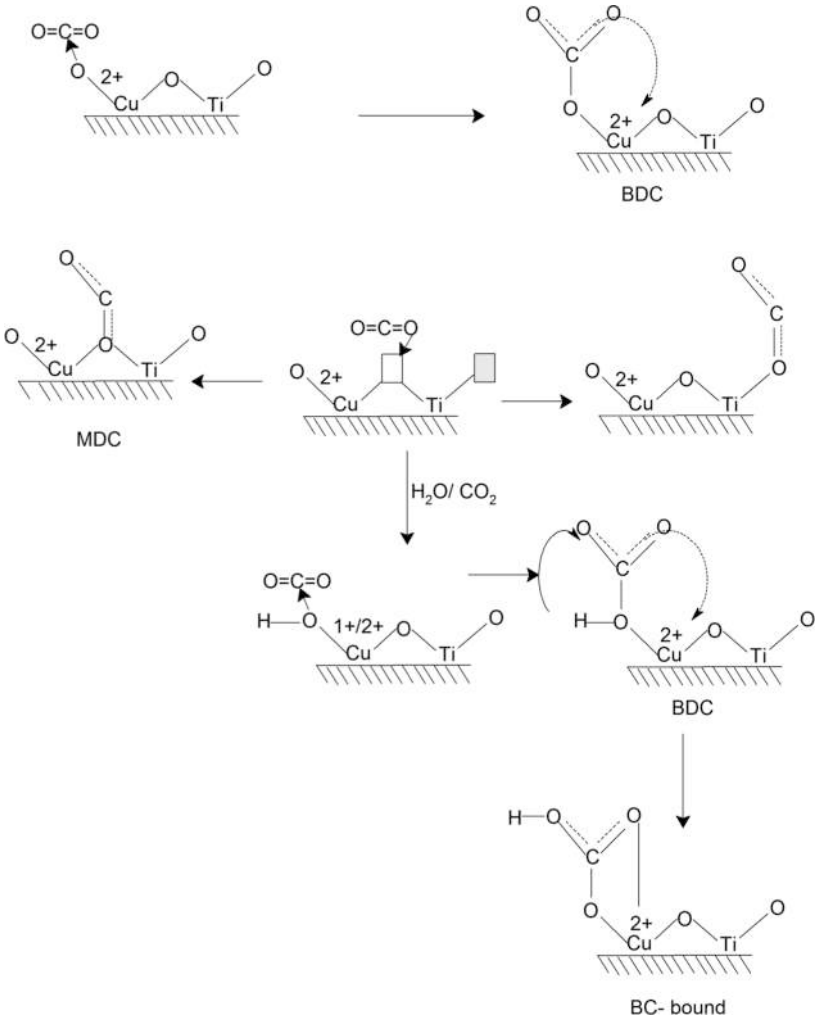

d EXAFS analysis shows the Cu−O bond lengths and coordination numbers do not vary significantly during the photocatalytic reduction of CO_2 for both Cu-5 and Cu-10 samples.

The valence band of the TiO_2 consists of Ti 4d and O 2p. An increment in the intensity of pre-edge peaks A1, A2, and A3 toward higher energy suggests distortion in the TiO_6 octahedra of anatase TiO_2, which can be formed as a result of higher orbital mixing between Ti and O,[59] resulting in the movement of electrons from VB to CB. The alteration of the Ti K-edge shows the decrease in coordination numbers, which shows the utilization of O vacancies in the photocatalytic process. However, the most salient feature is the shifting of charge for the Cu K-edge for both Cu-5 and Cu-10, signaling the fact that the electron transfer in Cu-based samples mostly occurs through Cu centers and not through the Ti centers, which shows the immense strength of the Cu-containing TiO_2 in the CO_2 reduction process. Another strange feature is that there is a very insignificant variation in the Cu−O bond length or coordination numbers during the photocatalytic reaction process. During the adsorption process, there is a clear alteration in the coordination number of Cu and Cu−O bond length, showing the adsorption intermediates are formed around Cu along with O vacancies. This also means that these intermediates are degraded to generate different intermediate species during the photocatalytic reaction to form either further intermediates or the final CH_4 product. Several studies have been carried out in order to understand the reaction mechanism involved during the photocatalytic reduction of CO_2[5]. Karamian et al.[61] have proposed some reaction mechanism of the photocatalytic reduction of CO_2 and tried to explain the effect of different reducing agents on the photocatalytic reduction process. Tan et al.[62] studied the photocatalytic reduction of CO_2 with TiO_2 pellets and proposed that the photogenerated electrons and holes are created on the surface of TiO_2. These charge carriers react with adsorbed water and CO_2, thus generating OH and carbon radicals. Carbon radicals are formed by the dissociation of CO_2 to CO as an intermediate, and H^+ ions are formed when the OH radicals further oxidize the water. The carbon radicals react with H^+ and electrons from the photocatalyst to form CH_4. Usually there are two different routes of showing the intermediates; the intermediates assigned for C2 and C3 are through the carbene model, and the formation of CH_4 is mainly through the formaldehyde/formic acid model.[5] The major intermediates obtained for adsorbed species for Cu-5 are mainly the carboxylates, which are predominantly transformed to formic acid and then to CO, which in turn explains the EXAFS inferences of the insignificant variation of the Cu−O bond length or coordination numbers in agreement with studies in previous literature.[63,64] The present study has helped to identify the different reaction intermediates formed during the reduction

https://doi.org/10.1021/acs.chemmater.4c00748
Chem. Mater. 2025, 37, 3927−3949

of CO_2 as well as effectively identifying the role of Cu in the photocatalyst.

In the present study, adsorption of CO_2 over O-vacancy sites near Cu and Ti (as depicted in the schemes above) shows that the electron in the oxygen vacancy defect sites can be transferred to the CO_2 molecules, resulting in the formation of CO_2^- species. The carboxylate species may decompose to CO, giving the extra oxygen to the vacancy site. This results in a decrease in the oxygen vacancy concentration as found from EXAFS results. Therefore, in addition to the earlier results of the formation of the CO from the carboxylate ions over Cu^{1+} in the case of TiO_2, it is mainly formed over the O vacancies formed near Ti^{4+}. The formation of CO from CO_2^- on decomposition has been confirmed by several other researchers also.[65−67] On the other hand, in the case of H_2O adsorption, more oxygen from the lattice diffuses to the surface, forming OH radicals, which results in the increase in oxygen vacancies. Many literature reports suggest that the Ti^{3+} cations present in the TiO_2 lattice also act as a site for adsorption.[67,68] However, in the present case, any change of effective charge of Ti cations during adsorption is not found. Therefore, it can be assumed that the oxygen vacancies near Ti^{4+} cations and not the Ti^{3+} cations participate in the adsorption process, as well as the photocatalytic process. The effective charge of the Cu cations increases during the adsorption of CO_2. This may be due to the transfer of electrons from surface Cu cations along with that from oxygen vacancy sites to the adsorbed CO_2 species, forming CO_2^- radicals. The effective charge on Cu, however, decreases during the adsorption of water vapor, which suggests that electrons are transferred to Cu cations during the process of generation of OH^- radicals.

On photoillumination, the Ti−O average coordination number decreases from 5.6 to 5.3 for the Cu-5 sample and from 5.6 to 5.4 for the Cu-10 sample. This suggests the generation of oxygen vacancies near the Ti cations on photoillumination. The partial regeneration of surface oxygen vacancies on the Cu/TiO_2 catalyst has also been observed by Liu et al.[66] The holes created in the TiO_2 lattice oxidize the surface oxygen atoms to O_2, thus forming oxygen vacancies. These defect sites are, however, further used for the activation and dissociation of CO_2 as discussed above, which results in a decrease in the oxygen vacancies as a function of time during the photoreduction of CO_2. The effective charge of Cu also decreases during photoillumination of the catalyst, which suggests the photogenerated electrons get transferred to the Cu cations. Thus, Cu acts as an electron-trapping agent in the TiO_2 lattice. The trapped electrons are transferred to the adsorbed CO_2 and result in the dissociation of CO_2. However, trapped electrons can also be transferred to H^+ or O_2. The transfer of electrons from Cu sites to the adsorbed species results in the reoxidation of Cu cations. This has been observed at certain time intervals when the effective charge of Cu increases, as shown in Figure 22. Liu et al.[66] have also found the formation of Cu^+-CO species during photoirradiation, which suggests the activation and dissociation of CO_2 at the Cu sites. Neatu et al.[67] have also found that Cu bonding to CO leads to the selective formation of CH_4. This is portrayed in Scheme 4.

3.9. Structure Activity Correlation. The intermediates upon exposure of CO_2 are BDC and BC, and upon adsorption of H_2O and CO_2, it is primarily BC. It establishes that in the presence of H_2O, the BDC species are converted to BC. The intermediates observed over reduced TiO_2 are mainly bicarbonates MDC and BDC but no carboxylates. The different

Scheme 4. Effect of the Cu Oxidation State and Role of Oxygen Vacancies in the Vicinity of Ti on Photocatalytic Activity in EXAFS/XANES Understanding

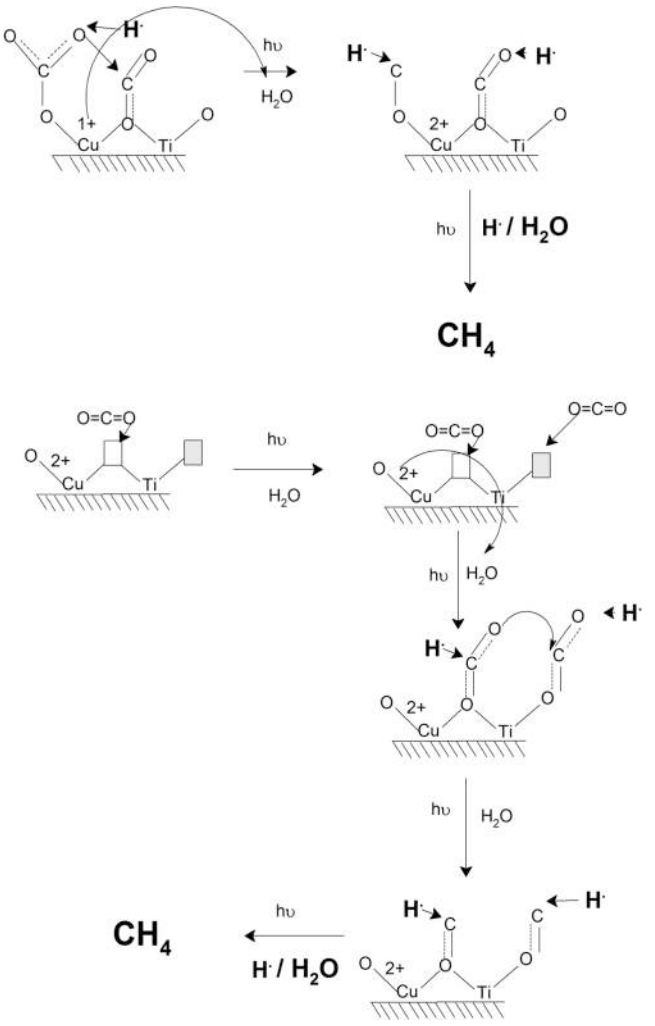

intermediates found for Cu-1 are MDCs and BCs on CO_2 reactive adsorption along with the formation of carboxylates, and upon H_2O and CO_2 exposure, the carboxylate intensity grows. The Cu-5 catalysts upon reactive adsorption of CO_2 form mainly BDC; however, the formation of BC and MDC is also observed. However, upon the adsorption of H_2O and CO_2, the formation of carboxylate and BCs and MDC and the carboxylate and BC species are stable in nature. The reactive adsorption of CO_2 and CO_2 and H_2O over the Cu-10 catalyst shows mainly the formation of BDCs and, in a small amount, MDCs and BCs, where postevacuation, the most stable are the BDCs, and BCs are formed. No carboxylates are observed, and very small amount of MDCs are produced, and this is explained in Schemes 1−3 by mainly the presence of Cu^{1+} and the O vacancy. The XPS-AES, XANES, and EELS structural studies show mainly the formation of two Cu-oxidation states as Cu^{1+} and Cu^{2+}, respectively. Table S3 shows the complete absence of Cu (0), and as a function of doping of Cu in the TiO_2 system, Cu^{1+} decreases. The EELS mapping along with the EXAFS data set and XPS studies shows definite formation of the O vacancy. The O vacancies are formed near Cu sites as well as near Ti^{4+} sites. Therefore, the presence of Cu^{1+} in the Cu-doped TiO_2 plays the strongest role for the different adsorbed intermediates formed.

https://doi.org/10.1021/acs.chemmater.4c00748
Chem. Mater. 2025, 37, 3927−3949

The XAS analysis at the Ti K-edge for Cu-5 and Cu-10 indicates that the effective charge of Ti cations does not change during the adsorption of CO_2 and water vapor. However, at the Cu K-edge, during the adsorption of CO_2 and water vapor on Cu-5 and Cu-10, it shows that the effective charge of Cu in the samples increases during CO_2 adsorption and decreases during H_2O adsorption, and it can be inferred that the Cu average coordination number decreases on adsorption of CO_2 and water vapor for both the samples. This implies the creation of oxygen vacancies near Cu cations due to both adsorptions of CO_2 and water vapor. Upon photocatalytic reaction, in situ EXAFS for the Ti K-edge shows the increase in average coordination numbers of the Ti as the reaction proceeds. However, the Ti−O and Ti−Ti bond lengths do not change significantly during the reaction. The Cu K-edge during the photocatalytic reduction of CO_2 with Cu-5 and Cu-10 shows that the absorption edge in general shifts toward lower energy with time during the photocatalytic reduction of CO_2 for both catalyst samples. From EXAFS analysis results, it can be seen that the Cu−O bond lengths and coordination numbers do not vary significantly during the photocatalytic reduction of CO_2 for both Cu5 and Cu10 samples, which is well explained in Scheme 4. The above can be explained in a very nice way with the presence of Cu^{1+}, whose concentration decreases with the percentage of Cu-doped TiO_2 and so does the photocatalytic activity (Table S3). Also, Cu-doping in the form of Cu^{1+} and Cu^{2+} will result in the formation of O vacancies to maintain the lattice charge. The more the amount of Cu^{1+}, the greater the amount of O vacancies, and they are used in the process of the photocatalysis. Therefore, in the photocatalytic activity, the Cu^{1+} state and O vacancy also plays a strong role and will vary as a result of their concentration in the Cu-doped TiO_2 system as a result of Cu-doping.

4. CONCLUSIONS

A mechanistic model is proposed to understand the role of Cu in the Cu-doped TiO_2 system and the photoreduction of CO_2 in the presence of moisture, which was taken up on a Cu-doped TiO_2 system, effectively resulting in the selective formation of only CH_4 upon exposure to CO_2 moisture and visible light. In situ FT-IR along with in situ XAS studies was used to understand the reactive adsorption of CO_2 and moisture over the different surfaces of these catalysts. The different factors affecting the different intermediates formed by reactive adsorption show the primary role of Cu, where the electron density around Cu and O vacancies would lead to the formation of carboxylates as intermediates. The extent of the back bonding of the adsorbed CO_2 over Cu^{2+}/Cu^{1+} would result in the formation of BDC or MDC strongly adsorbed or labile BCs that would affect the coordination number of Cu and the Cu−O bond length. It has been inferred from the Cu and Ti K-edge from XANES and EXAFS measurements that the oxygen vacancies present in the samples near the Ti cations and the Cu cations are the sites for CO_2 and water vapor adsorption in the catalysts. Upon illumination, the photogenerated electrons get transferred to the Cu cations, which act as electron traps in the TiO_2 lattice. The trapped electrons are transferred to the adsorbed CO_2 and result in the formation of CO_2^{-}·. On photoillumination, oxygen vacancies are also created in the lattice, which are further used for the activation and dissociation of CO_2 or H_2O. Therefore, in situ XAS along with in situ FT-IR measurement gives an understanding of the CO_2 and H_2O adsorption process on the Cu-doped TiO_2 catalyst and photoreduction of CO_2 to CH_4. Both Cu cations and oxygen vacancies present near Ti cations play important roles in the photoreduction of CO_2 to CH_4. The production of CH_4 during photocatalytic reduction of CO_2 has been confirmed by simultaneous gas chromatography (GC) measurements.

■ ASSOCIATED CONTENT

Supporting Information

The Supporting Information is available free of charge at https://pubs.acs.org/doi/10.1021/acs.chemmater.4c00748.

XRD patterns of nano-TiO_2, Cu-1, Cu-5, and Cu-10; cell parameter and crystallite size; XPS data of nano-TiO_2, Cu-1, Cu-5, and Cu-10 for Ti 2p, Cu 2p, and O 1s and deconvoluted data of respective XPS peaks to designate Cu^{1+}, Cu^{2+}, and O-vacancy states; deconvoluted spectra for Cu 2p for the samples Cu-1, Cu-5, and Cu-10; position and fwhm values for the Cu 2p in XPS; deconvoluted XPS spectra for Cu $2p_{3/2}$ XAES spectra for Cu $L_3M_{4,5}M_{4,5}$ in kinetic energy for the samples; concentration of CH_4 produced during the photocatalytic reduction of CO_2 during in situ XAS studies; in situ XANES spectra measured at the Cu K-edge of the Cu-5 and Cu-10 catalyst samples at some selected time intervals during the photocatalytic reduction of CO_2; TGA studies for the different Cu-doped TiO_2 samples to understand the stability of the catalysts up to 550 °C for $Ti_{1.99}Cu_{0.01}O_2$, $Ti_{1.95}Cu_{0.05}O_2$, and $Ti_{1.9}Cu_{0.1}O_2$; elemental analysis results of the samples using ICP-OES and XPS results; plot of the rate of CH_4 formation (μL/g/h) vs Cu-doping in the TiO_2 lattice and simultaneously plot of AQE for the same catalysts; concentration of Cu^{1+} and Cu^{2+} as a function of time with the Cu-5 sample from the XANES results; concentration of Cu^{1+} and Cu^{2+} as a function of time with the Cu-10 sample from the XANES results; plot of CH_4 (produced)/CO_2 (utilized) vs the time taken for the photoirradiation in the CO_2 photoreduction process of using the Cu-1 photocatalyst; EPR spectrum of different Cu-doped TiO_2 samples: Cu-1, Cu-5, and Cu-10 recorded at 96 K with an inset showing the Cu-doped TiO_2 samples at 298 K (RT) and another showing EPR for nana-TiO_2 at 96 K; and Raman spectra of the different samples: nano-TiO_2, Cu-1, Cu-5, and Cu10 (PDF)

■ AUTHOR INFORMATION

Corresponding Authors

Kaustava Bhattacharyya − *Chemistry Division, Bhabha Atomic Research Centre, Mumbai 400 085, India; Homi Bhabha National Institute, Mumbai 400 094, India;* orcid.org/0000-0003-4901-2814; Email: kaustava@barc.gov.in

Avesh K. Tyagi − *Chemistry Division, Bhabha Atomic Research Centre, Mumbai 400 085, India; Homi Bhabha National Institute, Mumbai 400 094, India;* orcid.org/0000-0002-4268-1364; Email: aktyagi@barc.gov.in

Authors

Chandrani Nayak − *Atomic and Molecular Physics Division, Bhabha Atomic Research Centre, Mumbai 400 085, India*

Dibyendyu Bhattacharyya − *Atomic and Molecular Physics Division, Bhabha Atomic Research Centre, Mumbai 400 085, India; Homi Bhabha National Institute, Mumbai 400 094, India;* orcid.org/0000-0002-1657-1858

https://doi.org/10.1021/acs.chemmater.4c00748
Chem. Mater. 2025, 37, 3927−3949

Ahin Roy − *Materials Science Centre, IIT-Kharagpur, Kharagpur 721302, India;* orcid.org/0000-0002-9515-2562

Complete contact information is available at: https://pubs.acs.org/10.1021/acs.chemmater.4c00748

Notes

The authors declare no competing financial interest.

■ ACKNOWLEDGMENTS

This manuscript is dedicated to Prof. C.N. R. Rao on his 90th birthday. One of the authors (AKT) sincerely acknowledges SERB for the J. C. Bose Fellowship (Grant Number: JCB/2023/000008). AR acknowledges funding from BRNS, DAE, Government of India. The electron microscopy was carried out at the HRTEM facility created and maintained by SATHI Foundation IIT Kharagpur. AR gratefully acknowledges the beam time in the state-of-the-art facility.

■ REFERENCES

(1) Fang, S.; Rahaman, M.; Bharti, J.; Reisner, E.; Robert, M.; Ozin, G. A.; Hu, Y. H. Photocatalytic CO_2 reduction. *Nat. Rev. Methods Primers* **2023**, *3* (1), 61.

(2) Lingampalli, S. R.; Ayyub, M. M.; Rao, C. N. R. Recent progress in the photocatalytic reduction of carbon dioxide. *ACS Omega* **2017**, *2* (6), 2740−2748.

(3) Kovacic, Z.; Likozar, B.; Hus, M. Photocatalytic CO_2 reduction: a review of ab initio mechanism, kinetics, and multiscale modeling simulations. *ACS Catal.* **2020**, *10* (24), 14984−15007.

(4) Kim, W.; Seok, T.; Choi, W. Nafion layer-enhanced photosynthetic conversion of CO_2 into hydrocarbons on TiO_2 nanoparticles. *Energy Environ. Sci.* **2012**, *5* (3), 6066−6070.

(5) Habisreutinger, S. N.; Schmidt-Mende, L.; Stolarczyk, J. K. Photocatalytic reduction of CO_2 on TiO_2 and other semiconductors. *Angew. Chem., Int. Ed.* **2013**, *52* (29), 7372−7408.

(6) Chen, Q.; Chen, X.; Fang, M.; Chen, J.; Li, Y.; Xie, Z.; Kuang, Q.; Zheng, L. Photo-induced Au−Pd alloying at TiO_2 {101} facets enables robust CO_2 photocatalytic reduction into hydrocarbon fuels. *J. Mater. Chem. A* **2019**, *7* (3), 1334−1340.

(7) Aguirre, M. E.; Zhou, R.; Eugene, A. J.; Guzman, M. I.; Grela, M. A. Cu_2O/TiO_2 heterostructures for CO_2 reduction through a direct Z-scheme: Protecting Cu_2O from photocorrosion. *Appl. Catal., B* **2017**, *217*, 485−493.

(8) Wang, Y.; Wang, W.; Mao, H.; Lu, Y.; Lu, J.; Huang, J.; Ye, Z.; Lu, B. Electrostatic self-assembly of $BiVO_4$−reduced graphene oxide nanocomposites for highly efficient visible light photocatalytic activities. *ACS Appl. Mater. Interfaces* **2014**, *6* (15), 12698−12706.

(9) Wang, S.; Wang, X. Photocatalytic CO_2 reduction by CdS promoted with a zeolitic imidazolate framework. *Appl. Catal., B* **2015**, *162*, 494−500.

(10) Wang, K.; Li, Q.; Liu, B.; Cheng, B.; Ho, W.; Yu, J. Sulfur-doped g-C_3N_4 with enhanced photocatalytic CO_2-reduction performance. *Appl. Catal., B* **2015**, *176*, 44−52.

(11) Zhang, X.; Han, F.; Shi, B.; Farsinezhad, S.; Dechaine, G. P.; Shankar, K. Photocatalytic conversion of diluted CO_2 into light hydrocarbons using periodically modulated multiwalled nanotube arrays. *Angew. Chem., Int. Ed.* **2012**, *51* (51), 12732−12735.

(12) Chen, G.; Gao, R.; Zhao, Y.; Li, Z.; Waterhouse, G. I. N.; Shi, R.; Zhao, J.; Zhang, M.; Shang, L.; Sheng, G.; et al. Alumina-supported CoFe alloy catalysts derived from layered-double-hydroxide nanosheets for efficient photothermal CO_2 hydrogenation to hydrocarbons. *Adv. Mater.* **2018**, *30* (3), 1704663.

(13) Wang, W.; Wang, L.; Su, W.; Xing, Y. Photocatalytic CO_2 reduction over copper-based materials: A review. *J. CO2 Util.* **2022**, *61*, 102056.

(14) Yin, G.; Nishikawa, M.; Nosaka, Y.; Srinivasan, N.; Atarashi, D.; Sakai, E.; Miyauchi, M. Photocatalytic carbon dioxide reduction by copper oxide nanocluster-grafted niobate nanosheets. *ACS Nano* **2015**, *9* (2), 2111−2119.

(15) Roy, S. C.; Varghese, O. K.; Paulose, M.; Grimes, C. A. Toward solar fuels: photocatalytic conversion of carbon dioxide to hydrocarbons. *ACS Nano* **2010**, *4* (3), 1259−1278.

(16) Zhu, S.; Liang, S.; Tong, Y.; An, X.; Long, J.; Fu, X.; Wang, X. Photocatalytic reduction of CO_2 with H_2O to CH_4 on Cu (I) supported TiO_2 nanosheets with defective {001} facets. *Phys. Chem. Chem. Phys.* **2015**, *17* (15), 9761−9770.

(17) Chen, J.; Iyemperumal, S. K.; Fenton, T.; Carl, A.; Grimm, R.; Li, G.; Deskins, N. A. Synergy between defects, photoexcited electrons, and supported single atom catalysts for CO_2 reduction. *ACS Catal.* **2018**, *8* (11), 10464−10478.

(18) Chen, B.-R.; Nguyen, V.-H.; Wu, J. C. S.; Martin, R.; Kočí, K. Production of renewable fuels by the photohydrogenation of CO_2: effect of the Cu species loaded onto TiO_2 photocatalysts. *Phys. Chem. Chem. Phys.* **2016**, *18* (6), 4942−4951.

(19) Tasbihi, M.; Kočí, K.; Troppová, I.; Edelmannová, M.; Reli, M.; Čapek, L.; Schomäcker, R. Photocatalytic reduction of carbon dioxide over Cu/TiO_2 photocatalysts. *Environ. Sci. Pollut. Res.* **2018**, *25*, 34903−34911.

(20) Liu, D.; Fernández, Y.; Ola, O.; Mackintosh, S.; Maroto-Valer, M.; Parlett, C. M. A.; Lee, A. F.; Wu, J. C. S. On the impact of Cu dispersion on CO_2 photoreduction over Cu/TiO_2. *Catal. Commun.* **2012**, *25*, 78−82.

(21) Park, S.-M.; Razzaq, A.; Park, Y. H.; Sorcar, S.; Park, Y.; Grimes, C. A.; In, S.-I. Hybrid Cu_xO−TiO_2 Heterostructured Composites for Photocatalytic CO2 Reduction into Methane Using Solar Irradiation: Sunlight into Fuel. *ACS Omega* **2016**, *1* (5), 868−875.

(22) Bhattacharyya, K.; Mane, G. P.; Rane, V.; Tripathi, A. K.; Tyagi, A. K. Selective CO_2 photoreduction with Cu-doped TiO_2 photocatalyst: delineating the crucial role of Cu-oxidation state and oxygen vacancies. *J. Phys. Chem. C* **2021**, *125* (3), 1793−1810.

(23) Tagawa, T.; Nomura, N.; Goto, S. In situ FTIR study on hydrogenation of carbon dioxide over titania-supported copper catalysts. *Appl. Catal., A* **1998**, *166* (2), 321−326.

(24) Wu, J. C. S.; Huang, C.-W. In situ DRIFTS study of photocatalytic CO_2 reduction under UV irradiation. *Front. Chem. Eng. China* **2010**, *4*, 120−126.

(25) Mino, L.; Spoto, G.; Ferrari, A. M. CO_2 capture by TiO_2 anatase surfaces: a combined DFT and FTIR study. *J. Phys. Chem. C* **2014**, *118* (43), 25016−25026.

(26) Bhattacharyya, K.; Danon, A.; Vijayan, B. K.; Gray, K. A.; Stair, P. C.; Weitz, E. Role of the surface lewis acid and base sites in the adsorption of CO_2 on titania nanotubes and platinized titania nanotubes: an in situ FT-IR study. *J. Phys. Chem. C* **2013**, *117* (24), 12661−12678.

(27) Raskó, J. FTIR study of the photoinduced dissociation of CO_2 on titania-supported noble metals. *Catal. Lett.* **1998**, *56* (1), 11−15.

(28) Debnath, S.; Song, X.; Fagiani, M. R.; Weichman, M. L.; Gao, M.; Maeda, S.; Taketsugu, T.; Schöllkopf, W.; Lyalin, A.; Neumark, D. M.; et al. CO_2 Adsorption on $Ti_3O_6^-$: A Novel Carbonate Binding Motif. *J. Phys. Chem. C* **2018**, *123* (13), 8439−8446.

(29) Fang, B.; Xing, Y.; Bonakdarpour, A.; Zhang, S.; Wilkinson, D. P. Hierarchical CuO−TiO_2 Hollow Microspheres for Highly Efficient Photodriven Reduction of CO_2 to CH_4. *ACS Sustainable Chem. Eng.* **2015**, *3* (10), 2381−2388.

(30) Camarillo, R.; Toston, S.; Martinez, F.; Jimenez, C.; Rincon, J. Enhancing the photocatalytic reduction of CO_2 through engineering of catalysts with high pressure technology: Pd/TiO_2 photocatalysts. *J. Supercrit. Fluids* **2017**, *123*, 18−27.

(31) Low, J.; Dai, B.; Tong, T.; Jiang, C.; Yu, J. In situ irradiated X-ray photoelectron spectroscopy investigation on a direct Z-scheme TiO_2/CdS composite film photocatalyst. *Adv. Mater.* **2019**, *31* (6), 1802981.

(32) Liu, Y.; Liu, D.; Wu, H.-H.; Fan, X.; Dou, A.; Zhang, Q.; Su, M. Improved cycling stability of Na-doped cathode materials

$Li_{1.2}Ni_{0.2}Mn_{0.6}O_2$ via a facile synthesis. *ACS Sustainable Chem. Eng.* **2018**, *6* (10), 13045−13055.
(33) Yang, G.; Chen, D.; Ding, H.; Feng, J.; Zhang, J. Z.; Zhu, Y.; Hamid, S.; Bahnemann, D. W. Well-designed 3D $ZnIn_2S_4$ nanosheets/TiO_2 nanobelts as direct Z-scheme photocatalysts for CO_2 photoreduction into renewable hydrocarbon fuel with high efficiency. *Appl. Catal., B* **2017**, *219*, 611−618.
(34) Kumar, A.; Kumar, A.; Krishnan, V. Perovskite oxide based materials for energy and environment-oriented photocatalysis. *ACS Catal.* **2020**, *10* (17), 10253−10315.
(35) Basu, S.; Nayak, C.; Yadav, A. K.; Agrawal, A.; Poswal, A. K.; Bhattacharyya, D.; Jha, S. N.; Sahoo, N. K. A comprehensive facility for EXAFS measurements at the INDUS-2 synchrotron source at RRCAT. *J. Phys.: Conf. Ser.* **2014**, *493*, 012032.
(36) Poswal, A. K.; Agrawal, A.; Yadav, A. K.; Nayak, C.; Basu, S.; Kane, S. R.; Garg, C. K.; Bhattachryya, D.; Jha, S. N.; Sahoo, N. K. Commissioning and first results of scanning type EXAFS beamline (BL-09) at INDUS-2 synchrotron source. *AIP Conf. Proc.* **2014**, *1591*, 649−651.
(37) Rasko, J.; Solymosi, F. Infrared spectroscopic study of the photoinduced activation of CO_2 on TiO_2 and Rh/TiO_2 catalysts. *J. Phys. Chem.* **1994**, *98* (29), 7147−7152.
(38) Liao, L. F.; Lien, C. F.; Shieh, D. L.; Chen, M. T.; Lin, J. L. FT-IR study of adsorption and photoassisted oxygen isotopic exchange of carbon monoxide, carbon dioxide, carbonate, and formate on TiO_2. *J. Phys. Chem. B* **2002**, *106* (43), 11240−11245.
(39) Zecchina, A.; Coluccia, S.; Guglielminotti, E.; Ghiotti, G. Infrared study of surface properties of. alpha.-chromia. I. Preparation and adsorption of water, heavy water, and carbon monoxide. *J. Phys. Chem.* **1971**, *75* (18), 2774−2783.
(40) Baltrusaitis, J.; Schuttlefield, J.; Zeitler, E.; Grassian, V. H. Carbon dioxide adsorption on oxide nanoparticle surfaces. *Chem. Eng. J.* **2011**, *170* (2−3), 471−481.
(41) Su, W.; Zhang, J.; Feng, Z.; Chen, T.; Ying, P.; Li, C. Surface phases of TiO_2 nanoparticles studied by UV Raman spectroscopy and FT-IR spectroscopy. *J. Phys. Chem. C* **2008**, *112* (20), 7710−7716.
(42) Yang, C.-C.; Yu, Y.-H.; van der Linden, B.; Wu, J. C. S.; Mul, G. Artificial photosynthesis over crystalline TiO_2-based catalysts: fact or fiction? *J. Am. Chem. Soc.* **2010**, *132* (24), 8398−8406.
(43) Bhattacharyya, K.; Varma, S.; Tripathi, A. K.; Bharadwaj, S. R.; Tyagi, A. K. Mechanistic insight by in situ FTIR for the gas phase photo-oxidation of ethylene by V-doped titania and nano titania. *J. Phys. Chem. B* **2009**, *113* (17), 5917−5928.
(44) Toledo-Antonio, J. A.; Capula, S.; Cortés-Jácome, M. A.; Angeles-Chávez, C.; López-Salinas, E.; Ferrat, G.; Navarrete, J.; Escobar, J. Low-temperature FTIR study of CO adsorption on titania nanotubes. *J. Phys. Chem. C* **2007**, *111* (29), 10799−10805.
(45) Amenomiya, Y.; Morikawa, Y.; Pleizier, G. Infrared spectroscopy of $C_{18}O_2$ on alumina. *J. Catal.* **1977**, *46* (3), 431−433.
(46) Peri, J. B. Infrared study of adsorption of carbon dioxide, hydrogen chloride, and other molecules on "acid" sites on dry silica—alumina and γ-alumina1. *J. Phys. Chem.* **1966**, *70* (10), 3168−3179.
(47) Parkyns, N. D. Influence of thermal pretreatment on the infrared spectrum of carbon dioxide adsorbed on alumina. *J. Phys. Chem.* **1971**, *75* (4), 526−531.
(48) Peri, J. B. Oxygen exchange between carbon dioxide (oxygen-18) and acidic oxide and zeolite catalysts. *J. Phys. Chem.* **1975**, *79* (15), 1582−1588.
(49) Baumgarten, E.; Zachos, A. Infrared spectroscopical investigations on the adsorption of CO_2 on aluminas and silica aluminas at elevated temperatures. *Spectrochim. Acta, Part A* **1981**, *37* (2), 93−98.
(50) Morterra, C.; Chiorino, A.; Boccuzzi, F.; Fisicaro, E. A spectroscopic study of anatase properties. *Z. Phys. Chem.* **1981**, *124* (2), 211−222.
(51) Tsuchiya, H.; Macak, J. M.; Müller, L.; Kunze, J.; Müller, F.; Greil, P.; Virtanen, S.; Schmuki, P. Hydroxyapatite growth on anodic TiO_2 nanotubes. *Journal of Biomedical Materials Research Part A* **2006**, *77* (3), 534−541.
(52) Bhattacharyya, K.; Danon, A.; Vijayan, B. K.; Gray, K. A.; Stair, P. C.; Weitz, E. Role of the Surface Lewis Acid and Base Sites in the Adsorption of CO_2 on Titania Nanotubes and Platinized Titania Nanotubes: An in Situ FT-IR Study. *J. Phys. Chem. C* **2013**, *117* (24), 12661−12678.
(53) Lopez, M. C.; Ortiz, G. F.; Lavela, P.; Tirado, J. L.; Stoyanova, R.; Zhecheva, E. Tunable Ti^{4+}/Ti^{3+} redox potential in the presence of iron and calcium in NASICON-type related phosphates as electrodes for lithium batteries. *Chem. Mater.* **2013**, *25* (20), 4025−4035.
(54) Angelome, P. C.; Andrini, L.; Calvo, M. E.; Requejo, F. G.; Bilmes, S. A.; Soler-Illia, G. J. A. A. Mesoporous anatase TiO_2 films: use of Ti K XANES for the quantification of the nanocrystalline character and substrate effects in the photocatalysis behavior. *J. Phys. Chem. C* **2007**, *111* (29), 10886−10893.
(55) Bunker, G. *A Practical Guide to X-Ray Absorption Fine Structure Spectroscopy*; Cambridge University Press Cambridge, 2010.
(56) Kelly, S. D.; Hesterberg, D.; Ravel, B. Analysis of soils and minerals using X-ray absorption spectroscopy. In *Methods of soil analysis part 5—mineralogical methods*; Soil Science Society of America, 2008; Vol. *5*, pp 387−463..
(57) Koningsberger, D. C.; Prins, R. *X-Ray Absorption: Principles, Applications, Techniques of EXAFS, SEXAFS and XANES Chemical analysis*; Wiley-Interscience, 1987; Vol. *92*.
(58) Lafont, U.; Carta, D.; Mountjoy, G.; Chadwick, A. V.; Kelder, E. M. In situ structural changes upon electrochemical lithium insertion in nanosized anatase TiO2. *J. Phys. Chem. C* **2010**, *114* (2), 1372−1378.
(59) Huang, K.; Sasaki, K.; Adzic, R. R.; Xing, Y. Increasing Pt oxygen reduction reaction activity and durability with a carbon-doped TiO_2 nanocoating catalyst support. *J. Mater. Chem.* **2012**, *22* (33), 16824−16832.
(60) Di Valentin, C.; Finazzi, E.; Pacchioni, G.; Selloni, A.; Livraghi, S.; Paganini, M. C.; Giamello, E. N-doped TiO_2: Theory and experiment. *Chem. Phys.* **2007**, *339* (1−3), 44−56.
(61) Karamian, E.; Sharifnia, S. On the general mechanism of photocatalytic reduction of CO_2. *J. CO2 Util.* **2016**, *16*, 194−203.
(62) Tan, S. S.; Zou, L.; Hu, E. Photocatalytic reduction of carbon dioxide into gaseous hydrocarbon using TiO_2 pellets. *Catal. Today* **2006**, *115* (1−4), 269−273.
(63) Liu, L.; Gao, F.; Zhao, H.; Li, Y. Tailoring Cu valence and oxygen vacancy in Cu/TiO_2 catalysts for enhanced CO_2 photoreduction efficiency. *Appl. Catal., B* **2013**, *134*, 349−358.
(64) Irie, H.; Kamiya, K.; Shibanuma, T.; Miura, S.; Tryk, D. A.; Yokoyama, T.; Hashimoto, K. Visible light-sensitive Cu (II)-grafted TiO_2 photocatalysts: activities and X-ray absorption fine structure analyses. *J. Phys. Chem. C* **2009**, *113* (24), 10761−10766.
(65) Li, Y.; Wang, W.-N.; Zhan, Z.; Woo, M.-H.; Wu, C.-Y.; Biswas, P. Photocatalytic reduction of CO_2 with H_2O on mesoporous silica supported Cu/TiO_2 catalysts. *Appl. Catal., B* **2010**, *100* (1−2), 386−392.
(66) Neatu, S.; Maciá-Agulló, J. A.; Concepción, P.; Garcia, H. Gold−copper nanoalloys supported on TiO_2 as photocatalysts for CO_2 reduction by water. *J. Am. Chem. Soc.* **2014**, *136* (45), 15969−15976.
(67) Liu, L.; Zhao, C.; Li, Y. Spontaneous dissociation of CO_2 to CO on defective surface of Cu (I)/TiO_{2-x} nanoparticles at room temperature. *J. Phys. Chem. C* **2012**, *116* (14), 7904−7912.
(68) Camarillo, R.; Tostón, S.; Martínez, F.; Jiménez, C.; Rincón, J. Improving the photo-reduction of CO_2 to fuels with catalysts synthesized under high pressure: Cu/TiO_3. *J. Chem. Technol. Biotechnol.* **2018**, *93* (5), 1237−1248.

https://doi.org/10.1021/acs.chemmater.4c00748
Chem. Mater. 2025, 37, 3927−3949